AST853/ASME470   Numerical Weather Prediction   Dr. Yuh-Lang Lin

Applied Sci & Tech PhD Program/Physics   ylin@ncat.edu

North Carolina A&T State University   http://mesolab.org

NWP Lecture Note 4

Numerical Modeling of Geophysical Fluid Systems

[Based on Chapter 13 Numerical Methods of "Mesoscale Dynamics" by Y.-L. Lin, 2007, Cambridge University Press]

Table of Contents

Lecture Note 4

➢ In Lecture Note 3, we have discussed various numerical approximations of the advection equation.

➢ However, to simulate a real geophysical fluid system, such as the atmosphere and ocean, we need to integrate a set of governing equations over a finite domain, which requires to choose domain size, grid size, time interval, total integration time, as well as to consider other factors, such as the initial condition, boundary conditions, etc.
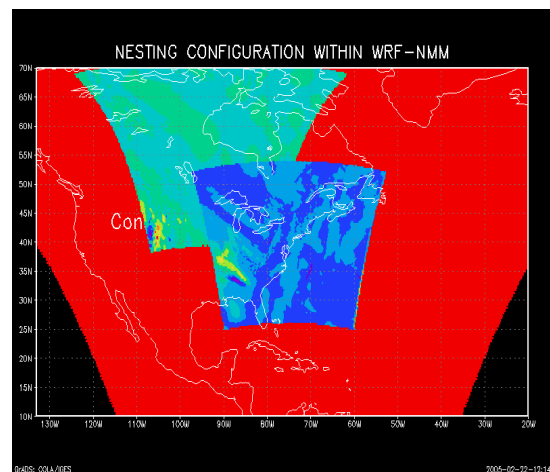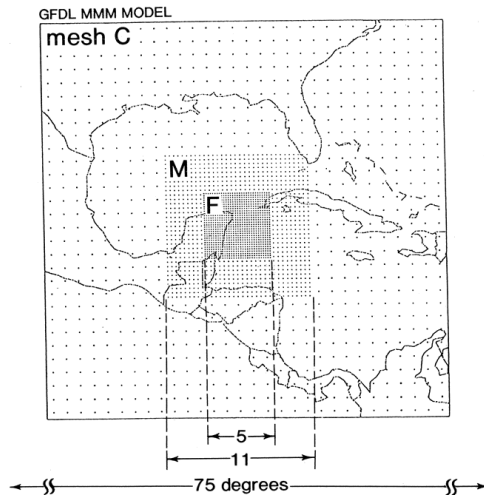
➢ In addition, when we deal with a real fluid system, the governing equations are much more complicated than the one-dimensional, linear advection equation, as considered in the previous chapter (Ch. 12),

$$\frac{\partial u}{\partial t} + c \frac{\partial u}{\partial x} = 0,$$
(12.3.1)

➢ For example, we have to integrate a set of 3D nonlinear governing equations with several dependent variables, instead of the 1D advection equation with only one variable.

$$\frac{du}{dt} = -\frac{1}{\rho}\frac{\partial p}{\partial x} + fv + F_{rx} \qquad (\text{x-momentum equation})$$

$$\frac{dv}{dt} = -\frac{1}{\rho}\frac{\partial p}{\partial y} - fu + F_{ry}$$
$$\qquad (\text{y-momentum equation})$$

$$\frac{dw}{dt} = -\frac{1}{\rho}\frac{\partial p}{\partial z} - g + F_{rz}$$
$$\qquad (\text{z-momentum equation})$$

$$\frac{d\rho}{dt} = -\rho\left(\frac{\partial u}{\partial x} + \frac{\partial v}{\partial y} + \frac{\partial w}{\partial z}\right)$$
$$\qquad (\text{Continuity equation})$$

$$\frac{dT}{dt} = Q$$
$$\qquad (\text{Thermo-energy Eq.})$$

$$p = \rho RT \qquad (\text{Equation of state})$$

➢ When a nonlinear equation is being approximated by numerical methods, one may face new problems, such as nonlinear computational instability and nonlinear aliasing, and numerical splitting. Special numerical techniques are needed to avoid this type of problems.

➢ Once optimal approximate forms of the equations are selected, however, it is still necessary to define the domain and grid structure over which the partial differential equations to be integrated.

➢ In this chapter (Ch. 13, Lin 2007), we will also discuss about how to build a numerical mesoscale model based on a set of partial differential equations governing a shallow water system, hydrostatic continuously stratified fluid system, and nonhydrostatic continuously stratified fluid system.

13.1 Grid Systems and Vertical Coordinates

➢ One important step in developing a numerical model to simulate a mesoscale system is to determine appropriate domain size, grid intervals, time interval, and total integration time of the model.

➢ Selection of the domain size, grid interval, total integration time and time interval in a mesoscale model is usually determined by both physical and numerical factors, such as:

    (1) Spatial scales and dimensionality of the forcing and physical processes
    (2) Time scales of the forcing and the fluid responses to the forcing
    (3) Limitations of predictability of the atmospheric phenomena
    (4) Stability criterion of the adopted numerical scheme
    (5) Availability of computer resources.

➢

➢ To represent mesoscale systems properly, it is required that:

(a) The meteorologically significant variations in the dependent variables caused by the mesoscale forcing and fluid responses are contained within the model, and

(b) The averaging volume used to define the model grid spacing must be sufficiently small, so that the mesoscale forcing and responses are accurately represented.

➢ In mesoscale modeling and numerical weather prediction, as well as general computational fluid dynamics, one needs to accurately represent multiscale processes in a finite domain.

➢ On one hand, it is important to capture the smaller-scale weather systems.

Thus, the grid and time intervals should be fine enough to resolve these small scale weather systems and processes.

➢ On the other hand, it is equally important to capture the larger-scale environment, which is responsible for the formation and modification of the small-scale weather system.

Therefore, model domain should be large enough to enclose the large-scale environment.

➢ Problems can arise if a domain is inappropriately selected.

For example, Fig. 13.1 shows some numerically simulated results of horizontal wind field for a hydrostatic flow over a bell-shaped mountain with a half-width of a and a height of h, $h(x) = h/(1 + (x/a)^2)$, but with 2 different domain sizes, $12a$ and $22.4a$.
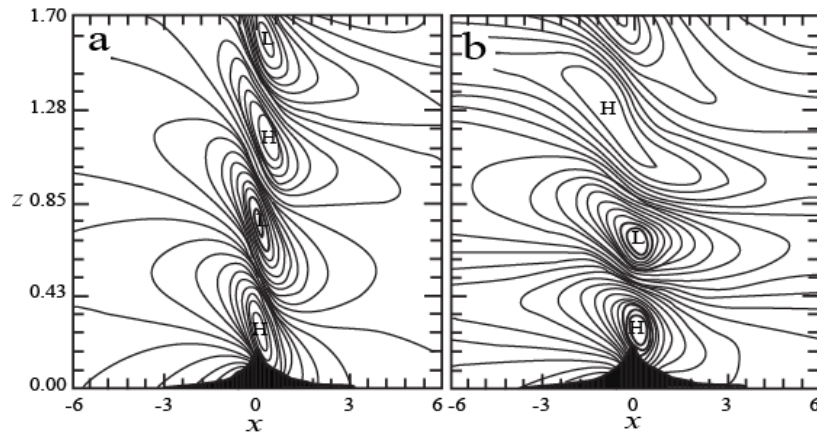

Fig. 13.1: Sensitivity of flow responses to the numerical domain size for a hydrostatic flow over a bell-shaped mountain. Displayed are the horizontal wind fields for different domain sizes: (a) $22.4a$ and (b) $12a$, where a is the half-width of the mountain. The abscissa and ordinate are non-dimensionalized by a and $2\pi U/N$ (vertical wavelength), respectively. The Froude number is 1.2 for both cases. (Lin and Wang 1996; Lin 2007)

In the figure, the horizontal axis is nondimensionalized by a, while the vertical axis is nondimensionalized by the hydrostatic vertical wavelength ($\lambda = 2\pi U/N$).

Both cases have the same *Froude number*, $F \equiv U/Nh = 1.2$, which is the only nondimensional control parameter for a two-dimensional, hydrostatic, nonrotating, inviscid flow past a mesoscale mountain, as discussed in Ch. 6.

The results have been strongly influenced by the domain size since the flow responses over the mountain are strongly

influenced by the upstream flow conditions at the left boundary of the numerical domain.

The upstream flow conditions, such as the basic horizontal wind and Brunt-Vaisala frequency, at the left boundary have been influenced by the upstream propagating disturbances generated by the orography.

Thus, if an inappropriate domain size is chosen to perform numerical simulations, the results may be contaminated by numerical factors.

The numerically simulated results are often verified by model intercomparison (e.g., Doyle et al. 2000 for MAP; Doyle 2011 for T-REX) and observations from field experiments.

➢ Once the domain size is chosen, the next natural step is to choose an appropriate grid size or grid interval.

The determination of the horizontal grid size used in a numerical model depends on spatial scales of the forcing, fluid responses, and numerical stability.

➢ The grid interval should well represent the forcing and fluid responses; otherwise the simulated results will not be accurate.

➢ After the domain size, grid interval and grid structure are chosen, the next step is to choose the time interval.

This is normally determined by the time variation of the forcing and stability criterion, which depends on the finite difference method or the numerical method adopted.

The linear stability criterion, as discussed in the last chapter, may serve, as a first guess of the time interval needed to guarantee the computational stability of the model.

As will be discussed later, nonlinear equations have a stricter criterion on computational stability, which is related to the time scale and the predictability of the weather phenomenon interested, and the computing resources available.

13.1.1 Grid Systems

➢ Different types of grid meshes may be adopted:

(a) *uniform grid mesh*,
(b) *stretched grid mesh*,
(c) *nested grid mesh*,
(d) *movable grid mesh*,
(e) *adaptive grid mesh*,
(f) *unstructured adaptive grid mesh*, and
(g) *staggered grid mesh*.

Some of them can be combined in a model.

➢ For a *uniform grid mesh*, grid intervals are set to be equal.

Advantages: easy to code onto a programming language and simple to input geographic features into the model.

Disadvantages: (1) it is difficult to properly incorporating both large and small features within the same model domain, (2) cannot resolve weather systems in areas need high resolution, (3) does not conserve mass.

For example, if one uses the same grid interval in vertical, it will be difficult to properly resolve the boundary layer circulation, while it is more than enough to resolve circulation in the free atmosphere (i.e., above the boundary layer), especially in the upper troposphere.

In general, uniform grid spacing at all levels is not feasible due to the limitation of computing speed.

➢ In the ***stretched grid mesh***, the grid intervals vary spatially.

Advantages: a much larger domain than the uniform grid mesh with the same number of grid points can be adopted for numerical simulations.

By adopting a grid mesh stretched from a finer resolution near the surface to a relatively coarse resolution in the upper troposphere and stratosphere allows a model to

resolve smaller-scale turbulent motions present in the planetary boundary layer.

Disadvantages:
(a) Difficult to code the finite difference equations onto the computer, and
(b) Reflections may occur if the grid intervals are stretched too much (Klemp and Lilly 1978).

In many mesoscale and NWP models, the vertical grid is often stretched. The vertical turbulent mixing provides a measure of needed grid resolution.

In general, mesoscale and NWP models have the smallest grid increments near the ground, because of the planetary boundary layer circulation, and the grid mesh stretches upward.
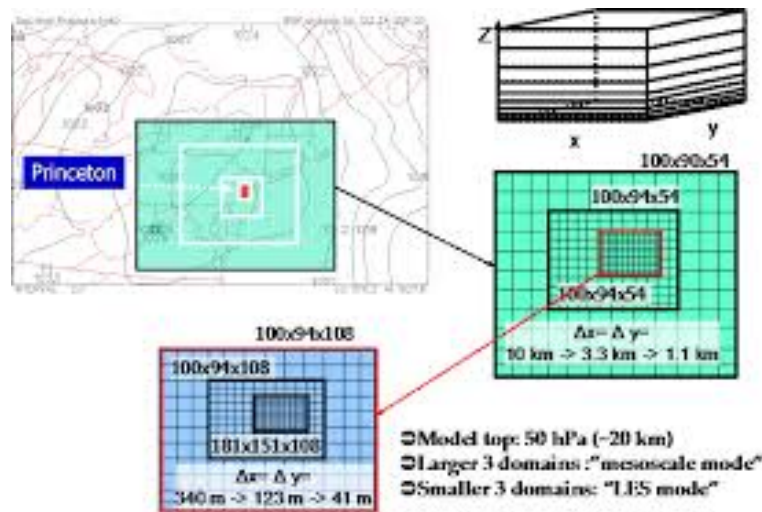
In order to avoid internal reflection from the internal boundaries, a smooth transition from the fine to coarse resolution is desirable.

The vertical stretch of the grid intervals may be defined by a known function, such as a logarithmic function, or specified by particular heights.

A ***two-way stretching*** may also be used. For example, in simulating flow with a critical level (z_c), where the basic wind speed equals to the phase speed of a propagating wave [$U(z_c) = c$], a much finer resolution is required to resolve the wave which has vertical wavelength approaching 0 in the vicinity of the critical level. Under this situation, one may need to define a stretching grid mesh having a very fine resolution near the critical level and stretches to coarser resolution both upward and downward.

➢ An alternative to the stretched grid approach is to insert a fine-mesh grid mesh, i.e. a ***nested grid mesh***, inside a coarse grid (see figure above (on p.12)).

In this way, it allows us to simulate the small-scale features, which are not resolvable by using the coarse grid mesh.

The coarse mesh provides the boundary conditions of the fine mesh.

Two types of grid nesting can be used in this type of grid meshes:

(i)   One-way nesting or parasitic grid representation: Only permit disturbances in the coarse grid mesh to enter the fine nested grid mesh.

(ii)   Two-way interaction: Permit disturbances to enter and leave the fine nested grid mesh.

Advantages: Allows smaller-scale weather systems and processes to be simulated without overstretching the computational time.

Disadvantages:
(1)   Inaccurate interface boundary conditions will lead to inaccurate numerical solutions in the inner domain (one-way nesting) or in both domains (two-way nesting).

(2)   The interaction among multiple nested meshes, particularly the tendency for propagating dispersive waves to discontinuously change their speeds upon passing from one mesh to the next and to reflect off the boundaries of each nested grid mesh, has been a topic of great concern (Dietachmayer and Droegemeier 1992).

➢ The above mentioned nested grid mesh can also be designed to move with a weather system (*movable grid mesh*), such as a cyclone, hurricane, front, or thunderstorm.

Advantages: it can follow the weather system and always provides a finer resolution needed in the vicinity of the weather system.

Disadvantages: One must know a priori, and for the duration of the calculation, which regions of the domain will require higher spatial resolution.

➢ To improve the nested grid and movable grid techniques, the *adaptive grid mesh* techniques have been proposed.

Grid points may be added in a structured manner through the placement of multiple and perhaps overlapping finer-scale grids in the domain (Berger and Oliger 1984).

➢ Fig. 13.2 shows one example of using 4 adaptive grid meshes to simulate the evolution of a density current produced by a prescribed cooling (Skamarock et al. 1989; Skamarock and Klemp 1993).
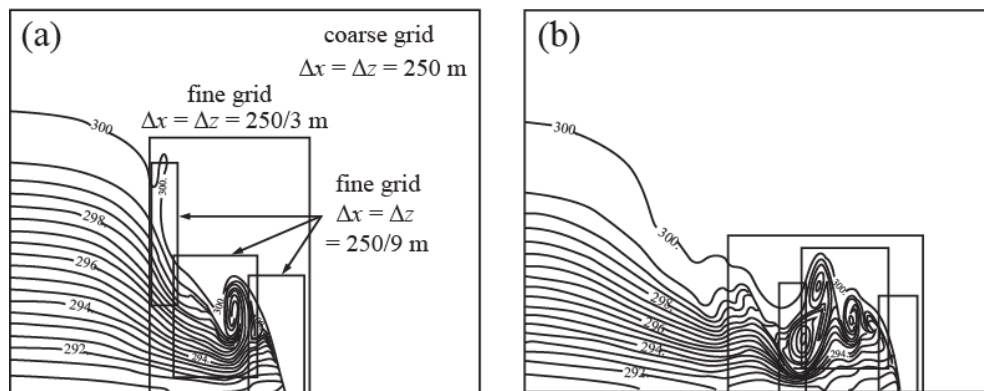

Fig. 13.2: Potential temperature fields at (a) 450 s and (b) 900 s in a cold pool collapse simulation using adaptive grid meshes. (After Skamarock 1989) [From Lin 2007]

➢ Regions of strong potential temperature gradients along the gust front and Kelvin-Helmholtz billows are well simulated.

➢ In the adaptive grid mesh, a fixed number of grid points or collocation points may also be redistributed in a predetermined manner to provide locally increased resolution and thus an improved solution in certain regions of the domain.

➢ Fig. 13.3 shows a simulation of kinematic frontogenesis, which is similar to a smoothed Rankine vortex being advected by a steady, nondivergent field, using this type of *structured continuous dynamic grid adaptation*.
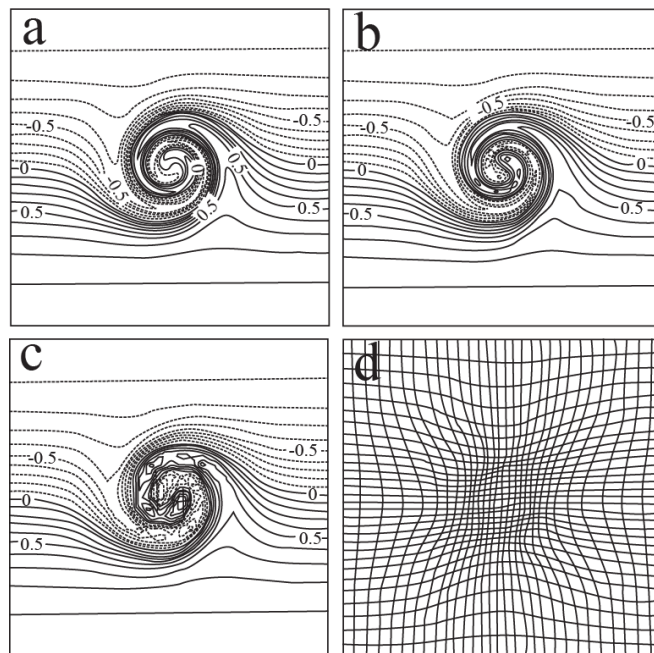
Fig. 13.3: (a) Exact solution of a passive scalar Q at t = 4 s for a kinematic frontogenesis being advected by a steady, nondivergent flow field with structure similar to that of a smoothed Rankine vortex (Doswell 1984). (b) Numerical solution for Q at t = 4 s on a fixed 31x31 uniform grid mesh. (c) Numerical solution for Q at t = 4 s using a continuous dynamic grid adaptation (CDGA). (d) Gridpoint distribution at t = 4 s with default parameters. (Adapted after Dietachmayer and Droegemeier 1992) [From Lin 2007]

➢ With both 31x31 grid points, the result (Fig. 13.3c) by using CDGA (Fig. 13.3d) is much better than that of uniform grid mesh (Fig. 13.3b), comparing with the exact solution (Fig. 13.3a).

➢ One *limitation* of this type of structured adaptive grid mesh is that it is not suitable for dynamic grid adaptation because the grid generation requires a high degree of user interaction and user expertise. Thus, it is not an easy task to apply this type of method for real-case simulations.

➢ In order to resolve the problem, the ***unstructured grid mesh*** has been proposed in dealing with both large- and small-scale features without having to engage nested grid mesh.

➢ One example is the unstructured grid mesh generated by the OMEGA model (Bacon et al. 2000), in which triangles are used as the base cells.
http://www.gulflink.osd.mil/al_muth/al_muth_refs/n58en096/overview.html

➢ One disadvantage of this approach is how to resolve the physics parameterization across various scales.
➢ Omega animations:
https://vortex.leidos.com/sims/hurricane/
➢ Newly adopted icosahedral-hexagonal grid by global NWP models (NOAA FV3, FIM & NIM models,
NCAR MPAS model).
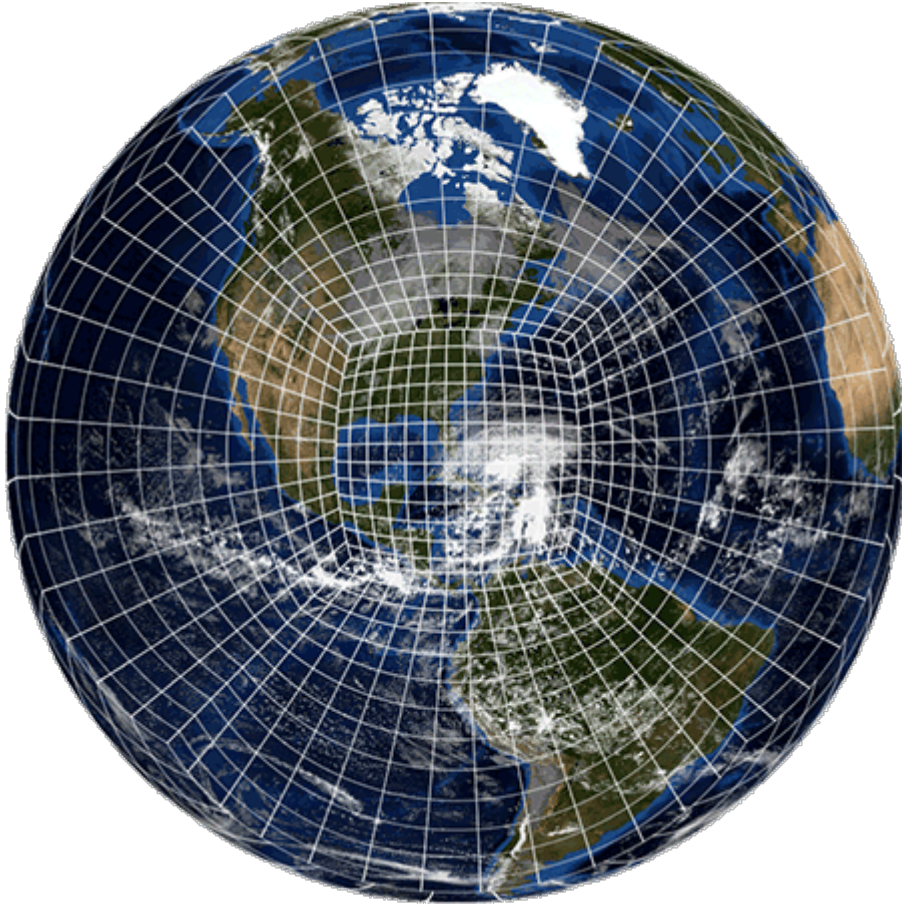
FV3 grid (an example)

(g) Staggered Grid Mesh

➢ When a system of governing equations with several unknown
variables, such as the shallow water system discussed in section 4.4
of Lin (2007), then the variables do not necessarily have to be defined
on the same grid points.

Instead, they can be staggered with respect to each other at different
grid points. This type of grid system is called *staggered grid mesh*,

which is motivated by the need to preserve some conservation relations.

- o For example, Lilly (1961) proposed a staggered grid system that helps preserve the total kinetic energy.
- o In this type of grid mesh, the variables are staggered with respect to each other.

➤ Consider the 2D incompressible continuity equation,

$$\frac{\partial u}{\partial x} + \frac{\partial w}{\partial z} = 0 .$$
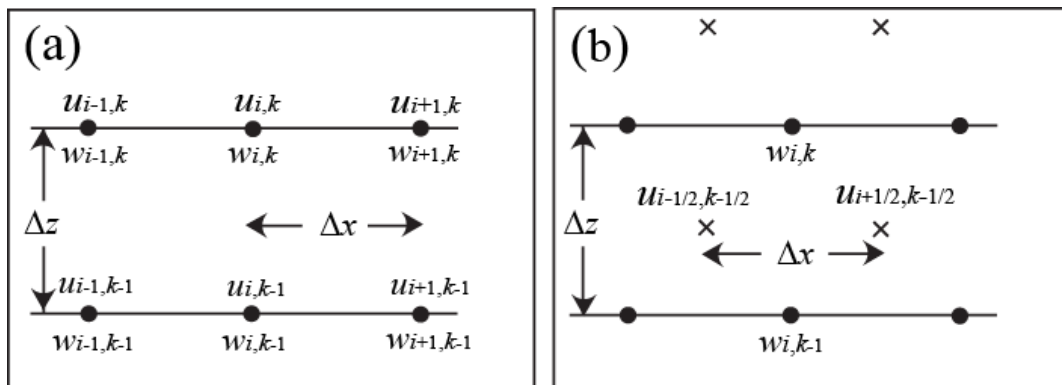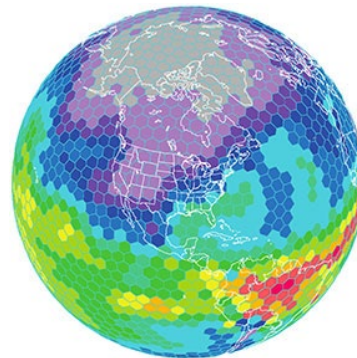(13.1.1)

Fig. 13.4: A schematic of (a) an unstaggered grid mesh and (b) a staggered grid mesh for the computation of u and w with the two-dimensional incompressible continuity equation.

Staggered grid in MPAS:

For an unstaggered grid mesh (Fig. 13.4a), a simple finite difference form may be written

$$w_{i,k} = w_{i,k-1} - \frac{u_{i+1,k-1/2} - u_{i-1,k-1/2}}{2\Delta x}\Delta z \;,$$

(13.1.2)

where

$$u_{i+1,k-1/2} = (u_{i+1,k} + u_{i+1,k-1})/2; \quad u_{i-1,k-1/2} = (u_{i-1,k} + u_{i-1,k-1})/2$$

(13.1.3)

For a staggered grid mesh (Fig. 13.4b), a simple finite difference form may be written

$$w_{i,k} = w_{i,k-1} - \frac{u_{i+1/2,k-1/2} - u_{i-1/2,k-1/2}}{\Delta x}\Delta z \;.$$

(13.1.4)

where u is defined to be located half-way between the grid points at which w is defined.

Thus, staggering the dependent variables as given by (13.1.4) increases the effective resolution by a factor of two, since derivatives are defined over an increment Δx, for instance, rather than $2\Delta x$, yet without requiring averaging as in (13.1.2).

➢ To examine the computational stability and phase characterics associated with a staggered grid mesh, we may consider applying the leapfrog in time and second-order centered difference scheme to the two-dimensional version of the

shallow water equations, Eqs. (4.4.21) and (4.4.23), with $U=0$ on a staggered grid mesh as shown in Fig. 13.5,
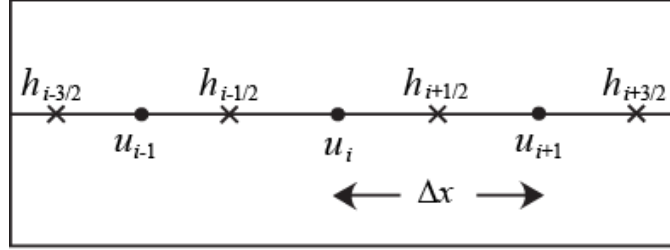
Fig. 13.5: A schematic of a staggered grid mesh for the shallow water system.

$$\frac{u_i^{\tau+1} - u_i^{\tau-1}}{2\Delta t} + g\frac{h_{i+1/2}^{\tau} - h_{i-1/2}^{\tau}}{\Delta x} = 0, \tag{13.1.5}$$

$$\frac{h_{i+1/2}^{\tau+1} - h_{i+1/2}^{\tau-1}}{2\Delta t} + H\frac{u_{i+1}^{\tau} - u_i^{\tau}}{\Delta x} = 0. \tag{13.1.6}$$

It can be derived that the computational or discrete dispersion relationship for the above system is

$$\sin \omega \Delta t = \pm \frac{2c\Delta t}{\Delta x}\sin\frac{k\Delta x}{2}, \tag{13.1.7}$$

where $c = \pm\sqrt{gH}$ are the shallow-water phase speeds. Since the solutions of the two-dimensional shallow water wave system are neutral, a real ω is required. Thus, a stable solution requires $|C| = |c\Delta t / \Delta x| \le 1/2$. It can also be derived that the stability criterion for an unstaggered grid mesh is $|C| \le 1$. Therefore, the maximum time interval for a staggered grid system is half of the corresponding unstaggered mesh system, which implies that the computational time is almost doubled.

This more stringent requirement on integration time interval may be compensated by an improved computational phase speed in using a staggered grid mesh, as shown in Fig. 13.6.
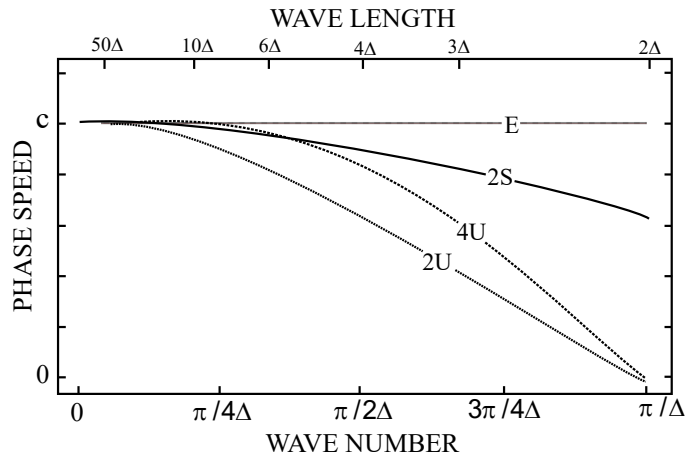
Fig. 13.6: Phase speed as a function of spatial resolution for the exact solution (E), for second-(2U) and fourth-order (4U) spatial derivative on an unstaggered grid mesh, and for second-order spatial derivatives on a staggered grid mesh (2S). Symbol Δ denotes one grid interval. (After Durran 1998, with kind permission of Springer Sciences and Media.) [Lin 2007]

Fig. 13.7 shows five grid meshes proposed by Arakawa and Lamb (1977). For staggered grid meshes, grid meshes B and C, which are often referred to as *Arakawa-B grid* and *Arakawa-C grid* in numerical modeling community, can better preserve the phase speed and group velocity (Fig. 13.7).
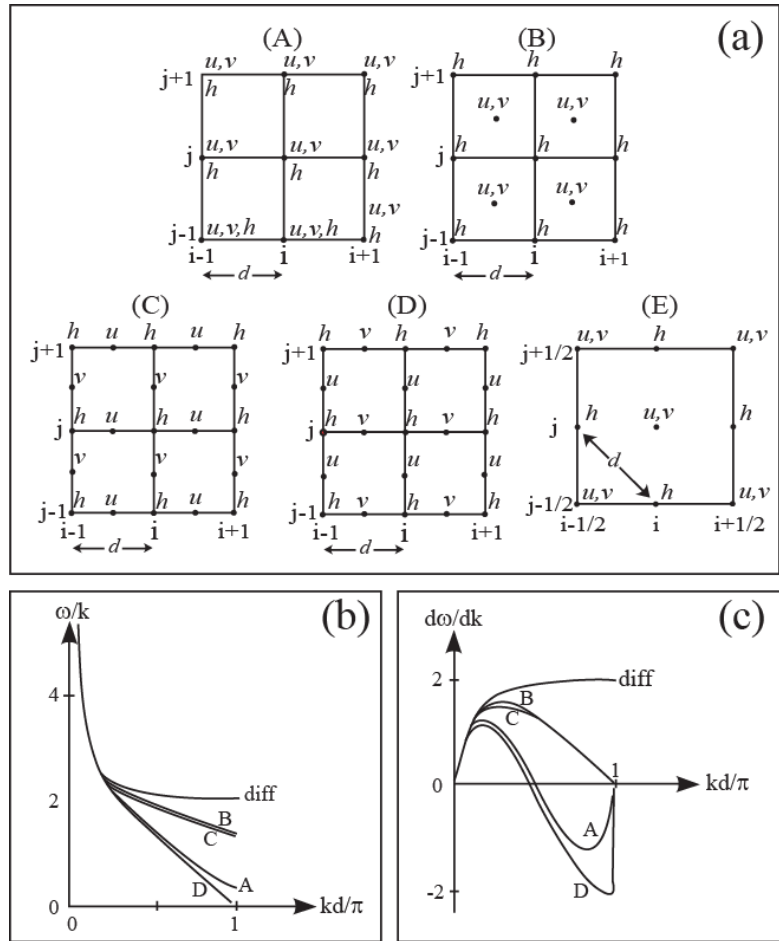
Fig. 13.7: (a) Five grid meshes proposed by Arakawa and Lamb (1977). The computational phase velocity ($c_p = \omega / k$) and the group velocity ($c_g = \partial\omega / \partial k$) analyzed as functions of kd / π for the four grids as shown in panels (b) and (c), respectively (Schoenstadt 1978). The differential equation solution is also included. These results use the following values: $\sqrt{gH} = 10^2\, ms^{-1}$, $f=10^{-4}$ s^{-1}, and d=500 m, where d is the grid interval depicted in panel (a). (Adapted after Arakawa and Lamb 1977)

- WRF adopted the Arakawa C grid system.
- Grid structure in MPAS:
file:///D:/Documents/1.2_NWP%20(EES753)/LECTURE%20NOTES/MPAS%20(grid%20struct ure.vert.coord.).htm

13.1.2 Vertical Coordinates

➤ In simulating a mesoscale flow in a finite domain, the height vertical coordinate may propose problems.

➤ For example, it may intercept the terrain in a mountainous area and creates a problem in dealing with the lower boundary condition.

Similar problems happen to the pressure coordinate and isentropic coordinate when isobaric surfaces and isentropic surfaces intercept the lower boundary, respectively. This may happen where there exists a blocking by the orography.

➤ To avoid the problem, Phillips (1957) proposed a vertical *sigma coordinate*, which matches the lowest coordinate surface with the bottom topography.

In this type of vertical $\sigma - p$ coordinates, the pressure coordinate is normalized by the surface pressure, p_s,

$$\sigma = \frac{p}{p_S} . \qquad\qquad (13.1.8)$$

Thus, $\sigma = 1$ at the surface and $\sigma = 0$ at the top of the atmosphere.

The σ vertical velocity, $\dot{\sigma} = D\sigma/Dt$, is 0 at both the surface and top of the atmosphere. In Eq. (13.1.8), σ may also be defined as

$$\sigma = \frac{p - p_S}{p_T - p_S} , \qquad\qquad (13.1.8)'$$

where p_T is the pressure at the top of the numerical domain.

The same concept may also be applied to the *isentropic coordinate*, in which σ may defined as

$$\sigma = \frac{\theta - \theta_S}{\theta_T - \theta_S}.$$
(13.1.9)

This type of coordinates is called $\sigma - \theta$ coordinates.

One of the advantages of the vertical isentropic coordinate is that it can resolve the vertical structure of weather systems, such as tropopause folding and upper-level frontogenesis.

When the sigma coordinate is applied to the height coordinates, it is called $\sigma - z$ or the terrain-following coordinates in which σ may be defined as

$$\sigma = \frac{z_T (z - z_S)}{z_T - z_S},$$
(13.1.10)

where z_S is the height of the lower surface in the $\sigma - z$ coordinate, which is independent of time, and z_T is a constant domain height or the constant height of the terrain-following part of the domain.

In a general σ coordinate, the pressure, p, may be written as

$$p(x, y, z, t) = p[x, y, \sigma(x, y, z, t), t].$$
(13.1.11)

The pressure gradient in x direction in the z coordinates may be obtained by performing the chain-rule,

$$\left(\frac{\partial p}{\partial x}\right)_z = \left(\frac{\partial p}{\partial x}\right)_\sigma + \frac{\partial p}{\partial \sigma}\left(\frac{\partial \sigma}{\partial x}\right)_z . \qquad (13.1.12)$$

If one replaces p by a general variable A, then the above transformation may be used to derive the gradient of A in x direction.

The pressure gradient $(\partial p / \partial x)$ in the σ coordinate may be obtained by deriving $(\partial \sigma / \partial x)_z$ from (13.1.10) and substituting it into (13.1.12),

$$\left(\frac{\partial p}{\partial x}\right)_\sigma = \left(\frac{\partial p}{\partial x}\right)_z - \left[\frac{\sigma - z_T}{z_T - z_S}\frac{\partial z_S}{\partial x}\right]\frac{\partial p}{\partial \sigma} .$$
(13.1.13)

Figure 2.1: ARW η coordinate.

➢ The Advanced Research WRF (ARW) model uses a terrain-following hydrostatic-pressure vertical coordinate (σ-p) (Skamarock et al. 2008).

$$\eta = \frac{p_h - p_{ht}}{p_{hs} - p_{hs}}$$

where p_h is the hydrostatic component of the pressure, and p_{hs} and p_{ht} refer to values along the surface and top boundaries, respectively. It was proposed by Laprise (1992).
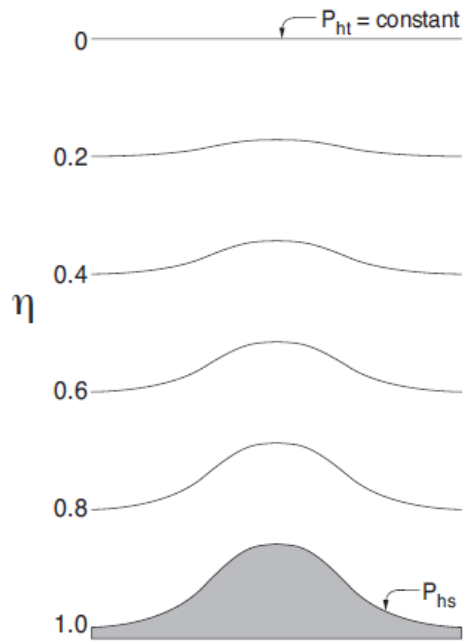
The boundary conditions assumed are *p=const* at the top boundary ($\eta=0$), and $\dot{\eta} = 0$ at $\eta=0$ and at the horizontal parts of the ground surface ($\eta = \eta_S$).

➢ One problem of the sigma vertical coordinate systems is that errors in two terms of the pressure gradient force do not cancel out (Smagorinski et al. 1967; also see the review in Mesinger and Janjic' 1985).

To avoid this problem, Mesinger et al. (1988) adopted a completely different vertical coordinate, the ***step-mountain*** or ***eta coordinate***, in the NCEP ETA model. In that model, *eta* (η) is defined as

$$\eta = \frac{p - p_T}{p_S - p_T}\eta_S \qquad (13.1.14)$$

With

$$\eta_S = \frac{p_{rf}(z_S) - p_T}{p_{rf}(0) - p_T}. \qquad (13.1.15)$$

➢ In the above equations, p is pressure; the subscripts T and S denote the top and surface values of the model atmosphere; z is geometric height, and $p_{rf}(z)$ is a suitably defined reference pressure as a function of z.

➢ A third method is to adopt a ***finite-element approximation*** of the governing equations, which simply approximate the mountain surface by one side of the finite elements.

There is no coordinate transformation needed in this approach. It has the same advantage of not having to transform the governing

equations into complicated forms as well as having a higher-order accuracy compared to the step-mountain coordinate.

Perhaps this is a better way to treat the lower-boundary condition; however, the finite-element method is a completely different method from the more popular finite-difference methods. This makes it difficult to apply if the model uses a finite difference method.

➢ So far, we have discussed about how to set the domain size, vertical and horizontal grid intervals, grid mesh and vertical coordinate.

However, we still need to find (a) the temporal values of variables at the beginning of the integration, and (b) the boundary values at a finite domain.

These are required by the fact that we are solving the initial-value and boundary-value problems mathematically.

13.2 Boundary Conditions

➢ To make the mathematical problem well posed, appropriate boundary conditions need to be specified in any limited-area models, such as mesoscale and numerical weather prediction models.

➢ If the model domain represents only part of the atmosphere in every direction, then boundary conditions are needed at the top, lateral, and lower boundaries of the model domain.

➢ Number of boundary conditions depends on the order of the differential equations in a particular direction involved.

13.2.1 Lateral Boundary Conditions

➢ The purpose of implementing the lateral boundary conditions is to allow the wave or disturbance to propagate out of or into the computational domain.

➢ The lateral boundary values need to be updated with time, in reflecting the time-dependent evolution of the real atmosphere outside the domain, so that the weather system may propagate into the nested domain.
e.g., simulation of a frontal passage over a finite domain.

➢ Basically, there are about five types of lateral boundary conditions used in mesoscale models:
(1) Closed or specified boundary conditions,
(2) Periodic boundary conditions,
(3) Time-dependent boundary conditions,
(4) Sponge boundary conditions, and
(5) Open or radiation boundary conditions.

(1) In the closed or specified lateral boundary conditions, the variables at the lateral boundaries are specified as either constant values or constant gradients, respectively.
   o The waves or disturbances generated within the domain may or may not propagate out of the domain if constant values or constant gradients have been specified.

- Normally, a *closed boundary condition* tends to reflect waves or disturbances generated within the domain back into it.
- Occasionally, it works if the lateral boundaries are far away from the generated disturbances or waves at the desired integration time, or there are no waves propagate toward a particular lateral boundary.

For example, a constant inflow boundary may work if it is consistent with the inflow speed of the physical system and the generated waves or disturbances are being advected by the inflow, so that they never reach the inflow (upstream) boundary.

Mathematically, this type of specified boundary condition is called Dirichlet boundary condition.

A constant gradient lateral boundary condition specifies a constant gradient, such as zero gradients (e.g., $\partial\phi/\partial x = 0$, ϕ is the variable concerned), at the lateral boundaries.

How effective is the *constant gradient lateral boundary condition* to propagate the waves out of the domain depends on how close of the specified constant gradients to the advection speed of the physical waves. This is also called Neumann boundary condition.
Numerically, a *zero-gradient lateral boundary condition* specifies $\phi_1^\tau = \phi_2^\tau$ and $\phi_N^\tau = \phi_{N-1}^\tau$ at boundary points *i=1* and *i=N.*

(2) A *periodic boundary condition* assumes all the variables at the right boundary are equal to the left boundary, i.e.

$\phi(x_N) = \phi(x_1)$. This type of boundary condition is adopted by the global model which split a certain longitude artificially for making numerical computation.

(3) A *time-dependent lateral boundary condition* is often adopted when numerical integration are performed concurrently at both the inner and outer domains, the lateral boundary values of the inner domain need to be specified by the updated values predicted by the outer domain. In this way, the weather systems, waves, or disturbances are able to propagate into the inner domain.

Otherwise, the simulations of the inner domain cannot reflect the larger-scale environmental changes with time. This is called the *one-way nesting*. In addition, if the lateral boundary values of the inner domain are passed back to the outer domain, then it is called the *two-way nesting*.

(4) A *sponge* or wave-*absorbing layer boundary condition* uses an enhanced filtering near the lateral boundaries to damp the waves or disturbances generated within the domain out of the lateral boundaries.

For example, Perkey and Kreitzberg (1976) formulated the sponge region as follows

$$\frac{\partial \phi_i}{\partial t} = W_i \left(\frac{\partial \phi_i}{\partial t} \right)_m + (1 - W_i) \left(\frac{\partial \phi_i}{\partial t} \right)_{ls}, \tag{13.2.1}$$

where m denotes the model calculated tendency of variable ϕ and ls denotes the larger scale specified tendency and W_i is given as follows:

$$
\begin{aligned}
W_i \ &= 0.0 \text{ for the (physical) boundaries} \\
&= 0.4 \text{ for the boundaries } \pm\Delta x \\
&= 0.7 \text{ for the boundaries } \pm 2\Delta x \\
&= 0.9 \text{ for the boundaries } \pm 3\Delta x \\
&= 1.0 \text{ for all the interior points.} \qquad (13.2.2)
\end{aligned}
$$

In <u>WRF</u>, the Lateral Boundary Conditions (linear in time) are
  – The wrfbdy file contains later gridded information at model points in a zone (e.g.) of 5 points wide around the domain
  – The boundary fields are linearly time-interpolated from boundary times to the current model time
  – This specifies the outer values, and is used to nudge the next 4 interior points

Israeli and Orzag (1981) examined both viscous and Rayleigh-damping absorbing layers for the linearized shallow-water system.

Klemp and Lilly (1978) examined the reflection produced by a wave-absorbing layer at upper boundary, which will be discussed in the upper boundary conditions.

(5) Radiation or open boundary conditions

For *pure gravity waves*, the horizontal phase velocity is directed in the same sense as the horizontal *group velocity*, such as shown in Eqs. (4.5.14a) and (4.5.15a), thus it is possible to use the advection equation to advect the *wave energy* out of the lateral boundaries.

Based on this concept, Orlanski (1976) has proposed the *open or radiation boundary condition* for a hyperbolic flow in a numerical model. For the outflow boundary, the radiation boundary condition may be written

$$\frac{\partial \phi}{\partial t} + (U + c_o^*)\frac{\partial \phi}{\partial x} = 0 \quad \text{at } x = L, \tag{13.2.3}$$

where $U + c_o^*$ is the propagation speed at the outflow boundary ($x=L$), which is to be determined. The leapfrog finite difference representation for time step $\tau\text{-}1$ of the above equation may be written

$$\frac{\phi_{b-1}^{\tau} - \phi_{b-1}^{\tau-2}}{2\Delta t} = \frac{-(U + c_o^*)}{\Delta x}\left(\phi_{b-1}^{\tau-1} - \phi_{b-2}^{\tau-1}\right). \tag{13.2.4}$$

Notice that the first term in the bracket of the right hand side is adopted to avoid numerical instability.

Based on the above approximation, the phase speed can be estimated by

$$U + c_o^* = -\frac{\Delta x}{2\Delta t}\left(\frac{\phi_{b-1}^{\tau} - \phi_{b-1}^{\tau-2}}{\phi_{b-1}^{\tau-1} - \phi_{b-2}^{\tau-1}}\right) \quad \text{evaluated at } b\text{-}1,$$

$$U + c_o^* = 0 \qquad \text{if R.H.S. of (13.2.5)} < 0,$$

$$U + c_o^* = \frac{\Delta x}{\Delta t} \qquad \text{if R.H.S. of (13.2.5)} > \Delta x / \Delta t \,, (13.2.5)$$

where subscript b denotes the boundary point and R.H.S. means the right-hand side.

For a hydrostatic and incompressible fluid system, since w is coupled with u, one may use the estimated phase speed of u for w.

This may also be applied to the coupled variables of potential temperature and pressure.

Once the phase speed is estimated, then the boundary value at time step $\tau + 1$ can be determined

$$\phi_b^{\tau+1} = \phi_b^{\tau-1} - \frac{2\Delta t}{\Delta x}(U + c_o^*)(\phi_b^\tau - \phi_{b-1}^\tau) \qquad (13.2.6)$$

where $U + c_o^*$ is estimated by Eq. (13.2.5). A similar formula can be formed for the inflow boundary.

$$\phi_b^{\tau+1} = \phi_b^{\tau-1} - \frac{2\Delta t}{\Delta x}(U - c_i^*)(\phi_{b+1}^\tau - \phi_b^\tau) \qquad (13.2.7)$$

Note that the specification of ϕ at both boundaries will lead to an overdetermined problem for the first-order advection equation.
In fact, this renders the problem ill-posed (Oliger and Sundström 1978). Nevertheless, Davies (1976, 1983) has suggested that wave-absorbing layers can have

considerable practical utility even when they require overspecification of the boundary conditions.

In practice, a *zero gradient lateral boundary condition* has been implemented as $\phi_N^{\tau+1} = \phi_{N-1}^{\tau}$.

This type of lateral boundary condition can be viewed as a special case of the radiation or open boundary condition because the wave propagating out of the right boundary is assumed to have a speed of $c = \Delta x / \Delta t$. If the real physical wave speed is very different from this numerical phase speed, then a large reflection from the boundary may occur.

➢ In WRF, the options for lateral boundary conditions are:

Lateral Boundary Condition Options

a. Periodic (*periodic_x / periodic_y*): for idealized cases.

b. Open (*open_xs, open_xe, open_ys, open_ye*): for idealized cases.

c. Symmetric (*symmetric_xs, symmetric_xe, symmetric_ys, symmetric_ye*): for idealized cases.

d. Specified (*specified*): for real-data cases. The first row and column are specified with external model values (*spec_zone* = 1, and it should not change). The rows and columns in *relax_zone* have values blended from an external model and WRF. The value of *relax_zone* may be changed, as long as *spec_bdy_width* = *spec_zone* + *relax_zone*. This can be used with *periodic_x* in tropical channel simulations.

   spec_exp: exponential multiplier for the relaxation zone ramp, used with a *specified* boundary condition. 0. = linear ramp, default; 0.33 = ~3*dx exp decay factor. This may be useful for long simulations.

e. Nested (*nested*): for real and idealized cases.

13.2.2 Upper boundary conditions

The upper boundary of a mesoscale or numerical weather prediction model should be placed as far as possible from the region with active mesoscale waves, convective systems, and weather disturbances.

Ideally, it should be placed at the top of the atmosphere, i.e. $p=0$. However, practically, it is impossible to do so due to the restriction of computing resources.

Depends on the weather systems simulated by the model, the top boundary of a numerical model domain may be placed at deep within the stratosphere, at the tropopause, or within the stable layer of the troposphere.

For example, a sea breeze circulation in a stable boundary layer normally does not penetrate to a high altitude, thus allows a top boundary of a mesoscale model to be placed at the mid-troposphere.

On the other hand, in simulating a flow over a mesoscale mountain, the mountain waves often can propagate to a very high altitude. Therefore, a much higher vertical domain is needed.

No matter how high the model domain extends in vertical, an appropriate upper boundary condition is still needed.

For example, the disturbances or waves generated by a mesoscale mountain in the lower stratosphere may look like very weak, the energy per unit area associated with them, which is proportional to N (e.g. see the vertical energy flux, Eq. (13.2.31) of Lin (2007), at later part of this subsection), may be as appreciable as the waves in the troposphere, which have much higher amplitudes, due to the strong stratification in the stratosphere.

➢ The addition of a *sponge layer* or *wave-absorbing layer* to the top of the *physical domain or layer* is a simple way to mimic the Sommerfeld (1949) radiation boundary condition in a numerical model.

The sponge layer is designed to damp out disturbances generated in the physical layer out of the upper boundary.

To elucidate the formulation of a sponge layer, we may consider the following steady-state, two-dimensional, linear, hydrostatic, nonrotating, Boussinesq flow with Rayleigh friction and Newtonian cooling added to the momentum and thermodynamic equations, respectively,

$$U\frac{\partial u'}{\partial x} + \frac{1}{\rho_o}\frac{\partial p'}{\partial x} = -\nu u', \tag{13.2.8}$$

$$\frac{\partial p'}{\partial z} - \left(\frac{g\rho_o}{\theta_o}\right)\theta' = 0, \tag{13.2.9}$$

$$\frac{\partial u'}{\partial x} + \frac{\partial w'}{\partial z} = 0, \tag{13.2.10}$$

$$U\frac{\partial \theta'}{\partial x} + \left(\frac{N^2\theta_o}{g}\right)w' = -\nu\theta'. \tag{13.2.11}$$

The above equations may be obtained from Eqs. (4.5.1)–(4.5.4).

To minimize reflections caused by rapid increases in viscosity, one may consider the following function (Klemp and Lilly 1978), which gradually increase ν from *0* at z_1 to ν_T at z_T,

$$v(z) = v_T \sin^2\left(\frac{\pi}{2}\frac{z-z_1}{z_T-z_1}\right), \qquad z_1 \le z \le z_T. \tag{13.2.12}$$

To investigate the properties of wave reflection from the wave-absorbing layer, we may assume a wave-like solution in x direction,

$$(u', w', p', \theta') = [\hat{u}(k,z), \hat{w}(k,z), \hat{p}(k,z), \hat{\theta}(k,z)] e^{ikx}. \tag{13.2.13}$$

Substituting the above equation into (13.2.8)-(13.2.11) yields

$$\hat{w}_{zz} + \frac{N^2}{U^2} \hat{w} = 0, \quad z \leq z_1, \tag{13.2.14a}$$

$$\hat{w}_{zz} + \frac{N^2}{U^2(1 - i\nu/kU)^2} \hat{w} = 0, \quad z_1 < z \leq z_T. \tag{13.2.14b}$$

The general solutions of the above equations may be written

$$\hat{w} = c_1 e^{il_1 z} + c_2 e^{-il_1 z}, \quad \text{for } z \leq z_1, \tag{13.2.15a}$$

$$\hat{w} = d_1 e^{il_2 z} + d_2 e^{-il_2 z}, \quad \text{for } z_1 \leq z \leq z_T, \tag{13.2.15b}$$

where

$$l_1 = \frac{N}{U} \quad \text{and} \quad l_2 = \frac{N}{U\sqrt{1 - i\nu/kU}}, \tag{13.2.16}$$

are the Scorer parameters for uniform basic flow (U) in the physical and sponge layers, respectively.

The four coefficients in Eq. (13.2.15) can be determined by the upper boundary condition, lower boundary condition, and two interface conditions at (i.e., w and w_z are continuous at z_1).

According to *Eliassen and Palm Theorem* (1960), c_1 term represents the upward propagation of the wave energy, while c_2 term represents the downward propagation of the wave energy. Thus, the ratio

$$r = \left| \frac{c_2}{c_1} \right|, \qquad\qquad (13.2.17)$$

represents the reflectivity produced by the upper viscous layer. Notice that r can be obtained after applying the interface conditions at $z = z_1$ and the boundary condition $\hat{w} = 0$ *at* $z = z_T$.

To minimize reflection from the upper boundary, Klemp and Lilly (1978) suggest that the depth of the sponge layer should be greater than the hydrostatic vertical wavelength ($\lambda = 2\pi U/N$) of the mesoscale disturbance.
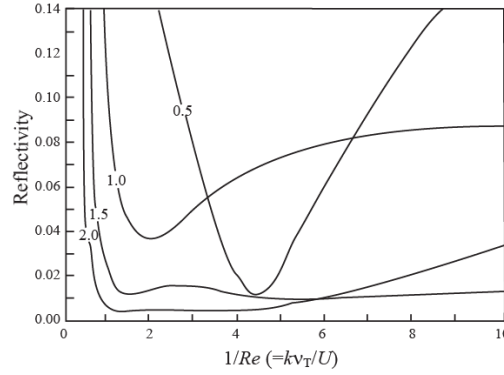

Fig. 13.8: Reflectivity, from the sponge layer as a function of a nondimensional inverse Reynolds number, 1/Re for several nondimensional sponge layer depths (d = 0.5, 1.0, 1.5, and 2.0). A value of r=1.0 corresponds to complete reflection from the top boundary of the computational domain. The nondimensional numbers are defined as $Re = U / k\nu_T$ and $d = (z_T - z_1)/\lambda$, where $\lambda = 2\pi U/N$. The viscosity coefficient is defined as $\nu = \nu_T \sin^2[\pi \ln(\bar{\theta}/\theta_1)/2\ln(\theta_T/\theta_1)]$, where θ_T and θ_1 are the potential temperatures at the top and bottom of the sponge layer, respectively. (Adapted after Klemp and Lilly 1978) [Lin 2007]

Nonlinear numerical experiments suggest that a sponge layer with a depth greater than 1.7λ is needed (Lin and Wang 1996, Lin 2007). Figure 13.8 shows the reflectivity from the sponge layer as a function of the nondimensional inverse Reynolds number, $1/\mathrm{Re} = k\nu_T/U$, where k is the horizontal wave number.

Numerical experiments performed by Klemp and Lilly (1978) also suggest that $v_T / v_1 < 6$ is a better choice to avoid the reflection due to the rapid increase of the coefficient of viscosity.

If the physical layer is assumed to be inviscid ($v_1 = 0$), one may choose $2 \le |v_T / kU| \le 5$, where k is the horizontal wave number. For example, we may choose $v_T = 0.002 \, s^{-1}$ for a basic flow with $U = 10 \, ms^{-1}$ over a bell-shaped mountain with $a = 20 \, km$.

Fig. 13.9 shows the results from a hydrostatic numerical model (panels a and b) using a sponge layer for flow over a bell-shaped mountain and compare with those calculated from Long's (1953) nonlinear theory. A vertical domain of $3.4\square$ is used, in which the upper half is the sponge layer. It can be clearly seen that the vertically propagating hydrostatic waves are effectively absorbed by the sponge layer.
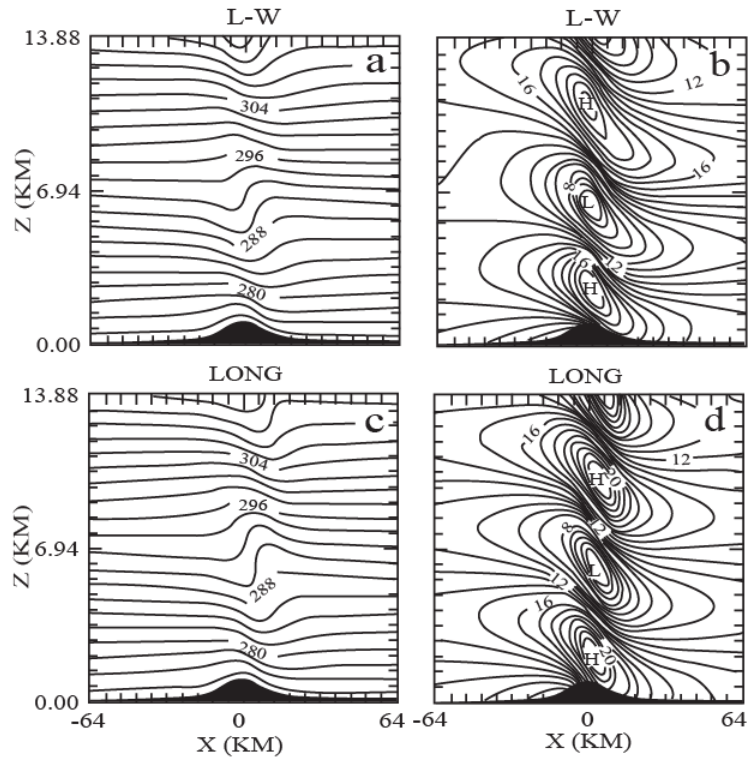
Fig. 13.9: Potential temperature ((a) and (c)) and total horizontal velocity fields ((b) and (d)) for a two-dimensional, continuously stratified, uniform flow over a bell-shaped mountain predicted at the nondimensional time $Ut/a = 100$ by a hydrostatic numerical model [(a) and (b)] and calculated by Long's steady state hydrostatic solution [(c) and (d)]. The Froude number ($F = U/Nh$) and hydrostatic parameter (Na/U) associated with the basic flow are 1.3 and 7.7, respectively. The dimensional flow and orographic parameters are $U = 13$ ms^{-1}, $N = 0.01$ s^{-1}, $h = 1$ km, and $a = 10$ km. The vertical coordinate is nondimensionalized by the hydrostatic wavelength $\lambda = 2\pi U/N$. (After Lin and Wang 1996) [Lin 2007]   (11/5/15)

➤ Radiation Upper Boundary Condition

Since the addition of a sponge layer increases the computational time significantly, a direct application of the Sommerfeld (1949) radiation condition has been proposed (Klemp and Durran 1983; Bougeault 1983).

To elucidate the numerical radiation boundary condition, we may consider the 2D, linear, hydrostatic, Boussinesq equations for a uniform basic state in the absence of Coriolis force:

$$\frac{\partial u'}{\partial t} + U\frac{\partial u'}{\partial x} + \frac{1}{\rho_o}\frac{\partial p'}{\partial x} = 0, \tag{13.2.18}$$

$$\frac{\partial p'}{\partial z} - \left(\frac{g\rho_o}{\theta_o}\right)\theta' = 0, \tag{13.2.19}$$

$$\frac{\partial u'}{\partial x} + \frac{\partial w'}{\partial z} = 0, \tag{13.2.20}$$

$$\frac{\partial \theta'}{\partial t} + U\frac{\partial \theta'}{\partial x} + \left(\frac{N^2\theta_o}{g}\right)w' = 0. \tag{13.2.21}$$

Again, we may assume a wave-like solution,

$$(u',w',p',\theta') = (u_o,w_o,p_o,\theta_o)\ e^{i(kx+mz-\omega t)}. \tag{13.2.22}$$

and substitute it into Eqs. (13.2.18)-(13.2.21) to yield the dispersion relation,

$$m^2(\omega - kU)^2 = N^2k^2. \tag{13.2.23}$$

From the above equation, the horizontal phase speed and the horizontal group velocity characterize the horizontal propagation of hydrostatic gravity waves,

$$c_{px} = \frac{\omega}{k} = U \pm \frac{N}{m}, \tag{13.2.24}$$

$$c_{gx} = \frac{\partial \omega}{\partial k} = U \pm \frac{N}{m}. \qquad (13.2.25)$$

Thus, for each wavenumber pair (k,m), the <u>horizontal propagation</u> speeds of the phase lines and energy are the same.

Consequently, the outward propagating wave energy can be transmitted through a lateral boundary by numerically advecting disturbances out of the boundary based on their horizontal phase speed, as proposed by Orlanski (1976) and discussed in Section 4.2.2.

Note that for nonhydrostatic waves, c_{px} and c_{gx} are not identical, however, they are still propagating in the same direction. Thus, the radiation or open lateral boundary condition is still able to advect the energy out by a simple advection equation.

In the vertical direction, the situation is completely different. For simplicity, we may assume $U = 0$. The phase speed and group velocity can be derived,

$$c_{pz} = \frac{\omega}{m} = \pm \frac{Nk}{m^2}, \qquad (13.2.26)$$

$$c_{gz} = \frac{\partial \omega}{\partial m} = \mp \frac{Nk}{m^2}. \qquad (13.2.27)$$

Notice that c_{pz} and c_{gz} have opposite signs, which imply that a positive (upward) c_{pz} will introduce downward energy propagation. Thus, we cannot use the advection equation to advect the wave energy generated within the domain out of the upper boundary, as that adopted by Orlanski (1976) for the radiation or open lateral boundary condition.

To identify wave modes with upward energy propagation, we consider linear disturbances of the form

$$\phi(x, z, t) = \hat{\phi}(k, z, \omega)e^{i(kx - \omega t)},$$
(13.2.28)

where ϕ may represent any dependent variables, u', w', p', or θ'. Substituting the above equation into the governing equation, (13.2.18)-(13.2.21), yields

$$\frac{\partial^2 \hat{w}}{\partial z^2} + \frac{N^2 k^2}{(kU - \omega)^2} \hat{w} = 0.$$
(13.2.29)

By assuming a positive k, the above equation has the following general solution,

$$\hat{w} = Ae^{iNz/(U - \omega/k)} + Be^{-iNz/(U - \omega/k)}.$$
(13.2.30)

A similar argument may also be made easily for a negative k. The vertical energy flux (Eliassen and Palm 1960) can then be obtained,

$$\overline{p'w'} = \frac{\rho_o N}{2k} \left(|A|^2 - |B|^2 \right),$$
(13.2.31)

where A and B terms represent the upward and downward propagation of wave energy, respectively. Thus, to avoid the wave reflection from the top boundary, we require $B=0$. Thus, for upward propagating waves, we choose

$$\hat{w} = Ae^{iNz/(U - \omega/k)}.$$
(13.2.32)

This implies

$$\frac{\partial \hat{w}}{\partial z} = \frac{iN}{U - \omega/k} \hat{w}.$$
(13.2.33)

From the continuity equation and momentum equation, we have

$$\frac{\partial \hat{w}}{\partial z} = -ik\hat{u} = \frac{ik / \rho_o}{U - \omega / k} \hat{p}. \tag{13.2.34}$$

If both positive and negative k are taken into account, then the above two equations lead to

$$\hat{p} = \frac{\rho_o N}{|k|} \hat{w} \quad \text{at} \quad z = z_T. \tag{13.2.35}$$

Since the above equation has no frequency dependence, we may write the above upper radiation condition in the wave number or Fourier space,

$$\tilde{p}(z,t) = \frac{\rho_o N}{|k|} \tilde{w}(z,t). \tag{13.2.36}$$

where $\tilde{p}$ and $\tilde{w}$ are defined as

$$(p, w) = (\tilde{p}, \tilde{w})e^{ikx} = (\hat{p}, \hat{w})e^{i(kx-\omega t)}. \tag{13.2.37}$$

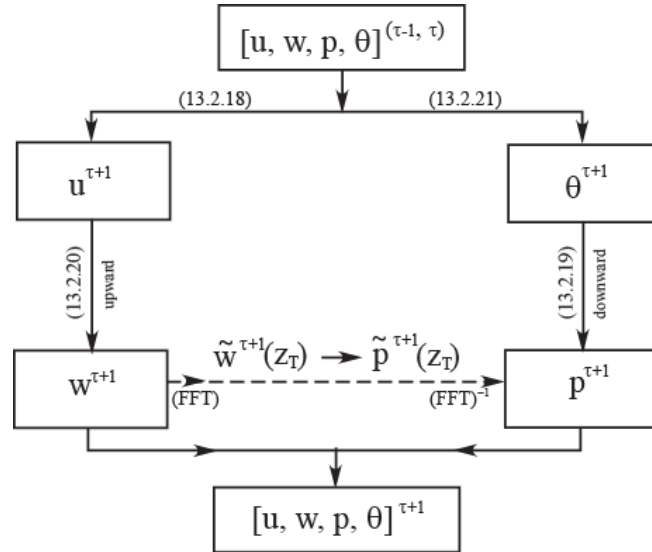➢ Numerical Implementation of the upper radiation boundary condition

Fig. 13.10: A flow chart for modeling the fluid flow system of (13.2.18) - (13.2.21) and implementing the numerical upper radiation boundary condition at the top of computational domain. FFT and FFT^{-1} denote the Fast Fourier Transform and the inverse Fast Fourier Transform.

➢ The numerical implementation of the upper radiation condition to the fluid flow system of Eqs. (13.2.18)-(13.2.21) may be sketched by Fig. 13.10. In the implementation procedure, the following five steps are taken:

(1) Integrate $w^{\tau+1}$ upward to z_T based on the continuity equation, Eq. (13.2.20).

(2) Make the Fourier transform of $w^{\tau+1}(z_T)$ to obtain $\widetilde{w}^{\tau+1}(z_T)$. A Fast Fourier Transform (FFT) numerical software may accelerate the computation.

(3) Apply Eq. (13.2.36) to obtain $\widetilde{p}^{\tau+1}(z_T)$.

(4) Make the inverse Fourier transform of $\widetilde{p}^{\tau+1}(z_T)$ to obtain $p^{\tau+1}(z_T)$

(5) Integrate hydrostatic equation downward based on the upper boundary condition of $p^{\tau+1}(z_T)$ to obtain $p^{\tau+1}(z)$ at every height level in the domain.

Klemp and Durran (1983) demonstrated that the upper radiation boundary condition is influenced by the nonlinearity of the fluid system.

Although the numerical radiation boundary condition is based more solidly on gravity wave theory, other factors, such as nonlinearity, nonhydrostaticity, and deep convection (which is not a wave) etc., may come into play in a more complicated fluid flow system.

In addition, the flow response is also sensitive to the domain height when an upper radiation boundary condition is implemented.

Options for upper boundary conditions in WRF
(Sec. 4.4, A description of ARW v3, NCAR)
- Absorbing Layer Using Spatial Filtering
- Implicit Rayleigh Damping for the Vertical Velocity
- Traditional Rayleigh Damping Layer

13.2.3 Lower Boundary Conditions

The lower boundary condition for an inviscid flow over a flat surface is that the flow near the surface is allowed to flow over it freely, which is often referred to as the *free-slip lower boundary condition*.

Since the normal velocity is required to be 0 at a rigid surface, the inviscid flow is always tangential to the surface.

For an inviscid flow over a mountainous terrain, the free-slip lower boundary condition requires the flow to be parallel to the surface.

For a two-dimensional flow, this requires

$$\frac{w}{u} = \frac{dh}{dx} \quad \text{at } z=h(x),$$ (13.2.38)

where $h(x)$ is the mountain profile.

The linear approximation of the above equation,

$$w' = (U + u')\frac{dh}{dx} \approx U\frac{dh}{dx} \quad \text{at } z=0,$$ (13.2.39)

has often been adopted in mountain wave theories.

In deriving the above equation, two nonlinearities have been neglected by assuming: (1) $u' \ll U$, and (2) the lower boundary condition is applied at $z=0$, instead of $z=h(x)$.

➢ For a three-dimensional flow, the linear lower boundary condition can also be derived,

$$w' = U\frac{\partial h}{\partial x} + V\frac{\partial h}{\partial y}.$$ (13.2.40)

Eqs. (13.2.39) and (13.2.40) are only valid for linear flow over small-amplitude mountains.

➢ In mesoscale numerical models, the inviscid lower boundary condition for flow over mountains is implicitly incorporated in the terrain-following (sigma) coordinates.

➢ With the planetary boundary layer considered, the *no-slip lower boundary condition* is should be implemented. That is,

$$u(z_o) = v(z_o) = w(z_o) = 0,$$
(13.2.41)

where z_o is the *roughness length*, which is defined as

$$u = (u_* / k)\ln(z / z_o).$$
(13.2.42)

In (13.4.42), k is a universal constant called the *von Karman constant* ($k \sim 0.4$ based on measurements) and u_* is the *friction velocity*, which can be obtained from the vertical momentum fluxes at surface,

$$u_* = \sqrt{\left(\overline{u'w'}\right)^2 + \left(\overline{v'w'}\right)^2},$$
(13.2.43)

where $\overline{u'w'}$ and $\overline{v'w'}$ are the turbulent momentum fluxes.

Measurements indicate that the magnitude of the surface momentum flux is of order $0.1\,m^2s^{-2}$. Thus, the friction velocity is typically of order $0.3\,ms^{-1}$.

➢ In addition to the specifications of the velocities, we also have to specify pressure and potential temperature.

The surface pressure may be specified based on hydrostatic balance, while the potential temperature may be prescribed as a periodic heating function,

$$\theta(z_o) = \theta_o(z_o) + \Delta\theta_{max} \sin(2\pi t / 24h) ,$$
(13.2.44)

where t is the time in hours after sunrise, $\theta_o(z_o)$ is the potential temperature at z_o at sunrise, and $\Delta\theta_{max}$ the maximum temperature attained during the day.

➤ To permit interactions between ground and the atmosphere, calculations of surface heat energy budget are needed. This is included in the parameterization of land surface processes.

➤ For flow over water surfaces, the air-sea interaction processes need to be considered, normally parameterized since most of the processes cannot be resolved by the models.

➤ Basically, the air-sea interactions work as the following.

a. The water influences the atmosphere through sensible and latent fluxes, which are related to the *sea surface temperature (SST)*.
b. The atmosphere influences the water or ocean through the wind stress to produce a deepening of the *ocean-mixed layer*, inducing water or ocean currents, and altering the *upwelling-downwelling* pattern.

13.3 Initial Conditions and Data Assimilation

➤ As mentioned earlier, mathematically the mesoscale modeling or numerical weather prediction (NWP) can be viewed as solving an initial-boundary value problem in which the governing equations

of geophysical fluid system are integrated forward in time in a finite domain.

➢ Therefore, in addition to the boundary conditions as discussed in the last section, we must also provide suitable initial conditions for the model.

➢ For idealized numerical simulations, the initial conditions may be prescribed by known functions or values.

    a. For example, the Advection Model and the Tank Model used or developed in the projects use known functions as the initial condition.

    Another example is that in making the model intercomparison for the Mesoscale Alpine Program (MAP), the participating numerical models use the same single sounding, which provides the vertical wind profile and temperature, of the 11 January 1972 Boulder, Colorado windstorm to initiate the models (Doyle et al. 2000).

    b. If the Coriolis force is included in the model, then the initial basic state should be in geostrophic balance. Otherwise, the initial state will be adjusted to reach a new balanced state by the model, which might not be the desired one.

➢ For real data mesoscale modeling or numerical weather prediction, the observational data must be modified to reduce errors and dynamically consistent with the governing equations of the model.

c. Strictly speaking, the process in producing initial conditions may be classified as the following four components:
   (i) *quality control*,
   (ii) *objective analysis*,
   (iii) *initialization*, and
   (iv) *initial guess from a short-range forecast by an NWP model*.

   These components have been taken to form a continuous cycle of data assimilation, often called *four-dimensional data assimilation* (4DDA).

d. A brief review of 4DDA may be found in *Lin* (2007), *Kalnay* (2003), *Daley* (1991), Harms et al. (1992) and Sashegyi and Madala (1994).

➤ The necessity of performing the *quality control* on meteorological data was recognized long ago, which is especially important when the data are used to initialize a NWP model.

e. Reason for quality control: The errors associated with the data may be misrepresented (*nonlinear aliasing*) and amplified by the model.

f. To reduce the errors in the sounding data, the following steps of quality control have been taken in numerical weather prediction (Gandin 1988):

   (a) *plausibility check*,
   (b) *contradiction check*,
   (c) *gross check*, and
   (d) *buddy check*.

In *plausibility check*, data values cannot possibly occur in the real atmosphere or extremely exceed climatological mean are rejected.

For example, positive temperatures in Celsius at 300 hPa are rejected.

In *contradiction check*, data values of two or more parameters at the same location contradicting to each other are removed.   For example, the occurrence of rain in the absence of clouds is removed.

In *gross check*, observations with large deviations from the first guess field forecast by an operational model are removed.

In *buddy check*, observations not agreeing with neighboring observations are removed.

➢ Observational data are often not regularly spaced, which are not ready for use as initial fields for a mesoscale or NWP model because they do not match the model grid mesh. In some areas, such as over ocean, observational data are sparse.

Therefore, in order to use the observational data as initial fields for a mesoscale or NWP model, one needs to interpolate or extrapolate the data to fit into the grid mesh of the model and to apply some balance relations, such as geostrophy and mass continuity, to make the data dynamically consistent.

This procedure is called *objective analysis*.

In an objective analysis, it is desirable to:

(1) Filter out scales of motion that cannot be resolved by the model,

(2) Use a first guess field or background field provided by an earlier forecast from the same model, which help avoid the extrapolation of observation data in data sparse areas and introduce dynamically consistency, and

(3) Make use of our knowledge of the probable errors associated with each observation, which may be weighted based on past records of accuracy.

When the maximum information from data sources, including the observations, climatological records, space correlation among the meteorological variables, etc., are extracted statistically, the approach is called *optimal interpolation*.

This often requires knowledge of the statistical structure of the fields of the variables. The variables may be analyzed separately or simultaneously, which is referred to as *univariate analysis* or *multivariate analysis*, respectively.

➢ The objective analysis procedure generally does not provide fields of mass and motion that are consistent with model dynamics to initiate a forecast.

Thus, the use of such objectively analyzed data to initialize an NWP model may generate large, spurious inertial-gravity wave modes.

Theoretically, these inertial-gravity wave modes will be dispersed, dissipated or propagate out of the domain due to redistribution of mass and wind fields.

However, these modes or noise, as often referred to by NWP modelers, cannot be dissipated locally because of the relatively low resolution in NWP models.

Therefore, an additional procedure, called *initialization*, is required to force the data after the objective analysis to be dynamically consistent with the model dynamics, and to allow the model to integrate forward in time with a minimum of noise and maximum accuracy of the forecasts.

Historically, a number of initialization techniques have been developed and used in mesoscale and NWP models, such as:

    (a) *damping method*,
    (b) *static initialization*,
    (c) *variational method*,
    (d) *normal mode initialization*, and
    (e) *dynamic initialization.*

Review of these methods can be found in Lin (2007) and Haltiner and Williams (1980).

➢ ***Damping method***
A simple and straightforward way to reducing the *gravity wave mode* is to dampen or filter the *inertial-gravity wave 'noise'* by adding a divergence damping term to the horizontal momentum equation (Talagrand 1972).

In this way, the local rate of change of the divergence will be diffused according to

$$\frac{\partial D}{\partial t} = -\frac{1}{\rho}\nabla^2 p + \nu\nabla^2 D + \dots \qquad (13.3.1)$$

This approach in initializing the data is called *damping method*.

➢ *Static initialization*
Another way to adjust the data at a single time level, usually to conform to some dynamical constraints in order to reduce or eliminate the generation of *inertial-gravity wave 'noise'* is the *static initialization.*

For example, in an isobaric model, one may
a. estimate the geopotential field (ϕ) from the pressure-height data and the geostrophic wind relations,
b. calculate the streamfunction (ψ) from analyzed ϕ fields on the isobaric surfaces, and then
c. compute the rotational wind component from the following relationship,

$$\boldsymbol{V}_\psi = k \times \nabla\psi , \qquad (13.3.2)$$

Eq. (13.3.2) may be written as an elliptic function of ϕ, which may become hyperbolic in some areas.

In order to insure ellipticity in these areas so that the numerical method for the elliptic equations will apply, the geopotential fields must be altered (Haltiner and Williams 1980).

In addition to this difficulty, the gravitational modes still exist even using the balance equation to determine a rotational wind for initialization.

➢ *Variational method*
Another approach to initializing the data is to adopt the *variational method,* in which one or more of the conservation relations are applied to minimize the variance of the difference between the observations and the objectively analyzed fields.

In performing the variational method, the concept of principles of variational calculus is applied (Sasaki, 1970).

For example, the difference may be minimized in a least-square sense subjected to one or more dynamical constraints, such as the balance equation, hydrostatic relation, and steady state momentum equation.

The static initialization described above is based on the distinction between gravity wave modes with relatively high divergence and other meteorological modes of the quasi-geostrophic type with small divergence and relatively high vorticity.

➢ *Normal mode initialization*
However, in reality the separation between gravity wave modes and other meteorological modes is far less clear cut in some occasions. Thus, it has been proposed to keep some normal modes if they can be represented by the model grid resolution.

Retaining these gravity wave modes are important since some severe weather have been found to be induced by gravity waves (e.g., Uccellini 1975; Kaplan et al., Koch et al. – see Lin 2007 for references).

Unlike applying the balance equation constraint, the *normal mode initialization* produces a divergent component as well.

Thus, this type of normal mode initialization makes an optimal use of the observed data by adjusting both mass and motion fields while achieving dynamical consistency through appropriate constraints.

In the *linear normal mode initialization* the original objectively analyzed fields are adjusted to the linearized versions of the model equations and the undesirable gravity wave modes are removed.

However, the disadvantage of this type of method is that nonlinear terms tend to regenerate the high-frequency wave modes, and also the curvature in the flow is neglected so that the fit with the original data may suffer. This is overcome by taking the *nonlinear normal mode initialization* technique (Machenhauser 1977; Baer 1977).

In the nonlinear normal mode initialization, the tendency of the undesirable wave modes, instead of the amplitude, is set

to zero. The nonlinear normal mode initialization may also be applied to the vertical direction, too.

Fig. 13.11 shows the time evolution of a height field after applying two iterations of the *implicit normal mode initialization* scheme (Temperton 1988).
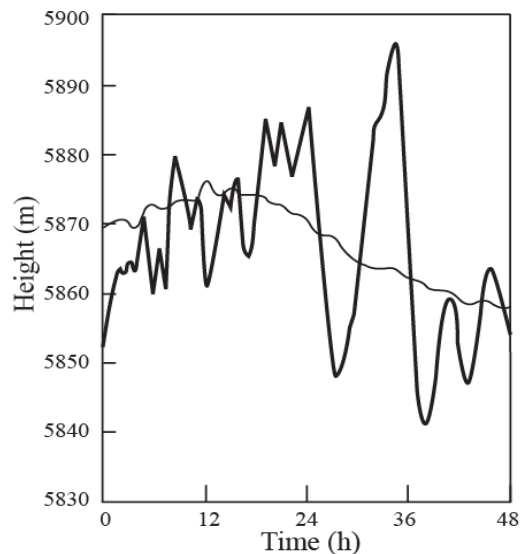
Fig. 13.11: Time evolution of height field after two iterations of the implicit nonlinear normal mode initialization scheme (thin curve) and with no initialization (bold curve). (After Temperton 1988)

Comparing with the time evolution of the same height field with no initialization, the implicit nonlinear normal mode initialization appears to be able to remove high-frequency oscillations.

Dynamic initialization
Since the normal mode initialization is performed separately right after the objective analysis, the initialized

fields may no longer fit the observations as closely as possible. Therefore, the *dynamic initialization* is proposed (Miyakoda and Moyer 1968).

The basic idea of dynamic initialization is to let the NWP or mesoscale model to do the job by itself because any primitive equation models are supposed to inherently possess the mechanism for the geostrophic adjustment process.

Indeed, the mass and velocity fields do mutually adjust to each other toward a quasi-geostrophic state when they are executed in an NWP model.

In this way, observations are inserted intermittently or continuously over a period of time. In this type of initialization, the model is integrated forward and backward about the initial time and let the model adjust itself before starting the forecast.

During this process, it may be desirable to use an integration scheme with selective damping technique, such as the Lax-Wendroff (see Ch. 14) or the Euler-backward scheme (e.g., see Haltiner and Williams 1980; Lin 2007). For example, the iterative scheme by Okamura (see Temperton, 1976) consists of a forward step, then a backward step and finally an averaging.

$$u_*^{\tau+1} = u^{\tau} + \Delta t(\partial u / \partial t)^{\tau},$$

$$u_{**}^{\tau} = u_*^{\tau+1} - \Delta t(\partial u_* / \partial t)^{\tau+1}, \qquad (13.3.3)$$

$$\overline{u}^{\tau} = 3u^{\tau} - 2u_{**}^{\tau}.$$

Fig. 13.12: Gravity wave activity after normal mode initialization, dynamic initialization for five vertical modes of a baroclinic model, and compared to that with no initialization. Note that the gravity wave activity is dramatically reduced by dynamic initialization. (Adapted after Sugi 1986)
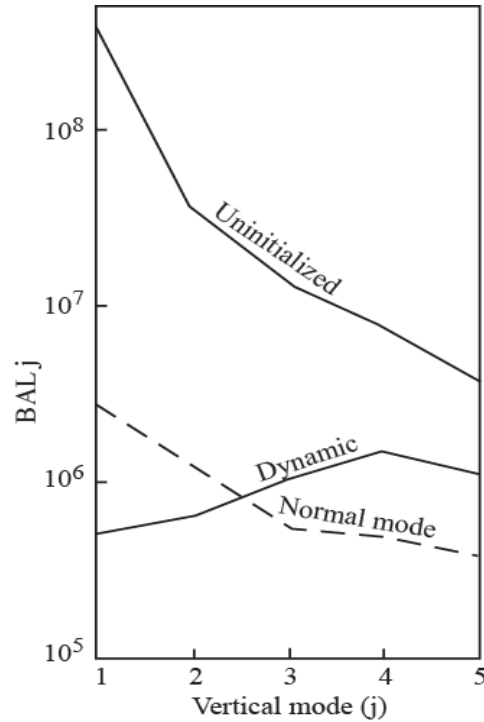
Fig. 13.12 shows an example of gravity wave activity after normal mode initialization and dynamic initialization for five vertical modes of a baroclinic model, and compared with that with no initialization (Sugi 1986). Low gravity wave modes (small j in the figure) are dramatically reduced by the dynamic initialization.

The disadvantages of the dynamic initialization scheme are that:

(i)   Each iteration requires the equivalent of two prognostic steps. To dampen the gravitational noise sufficiently would require much iteration that would take considerable computer time,

(ii) Dynamic initialization is unable to distinguish between large-scale gravity wave modes and small-scale Rossby modes, and

(iii) Backward integration may not be applicable to some irreversible physical processes.

➢ ***Four-Dimensional Data Assimilation (4DDA)***

- In 4DDA, the invaluable asynoptic data, such as NEXRAD (NEXt Generation RADar) Doppler radar, wind profilers, acoustic sounders, high-resolution dropsondes, satellite and aircraft, observed at nonstandard time (i.e., not at 00Z and 12Z) are inserted into an NWP model system, the quality control, objective analysis, initialization, and initial guess forecast from the same model are combined into the 4DDA cycle.

- The 4DDA cycle may be carried out in an intermittent or continuous fashion.

- In the *intermittent 4DDA,* the data are assimilated intermittently at specified time intervals. The background or first guess fields forecast by the model plays a very important role, especially in data sparse regions.

- In data rich regions, usually the analysis is dominated by the information contained in the observations. The boundary conditions of regional NWP are provided by global model forecast.

- The intermittent 4DDA techniques, such as three-dimensional variational data assimilation (3DVAR), are used in most present day global and regional operational NWP systems due to its computational efficiency.
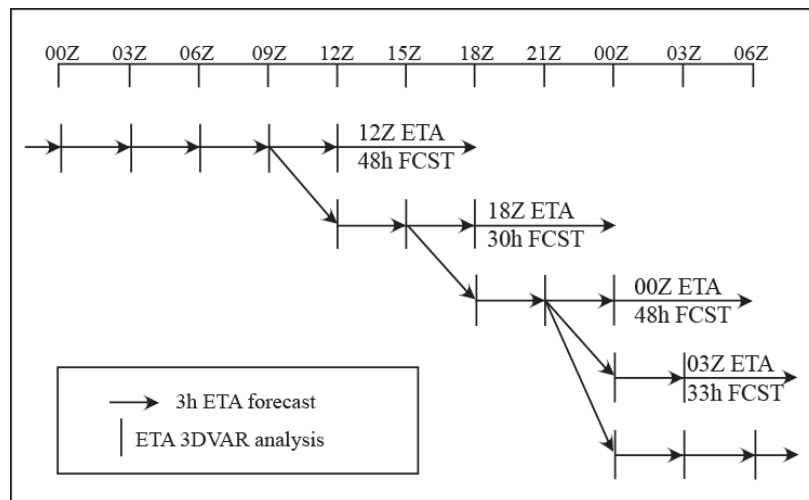

Fig. 13.13: An example of data assimilation cycle adopted by NCEP's ETA model by using 3DVAR technique. (Adapted after Rogers et al. 1998)

Fig. 13.13 illustrates a 32-km EDAS (Eta Data Analysis System, see Parrish et al. 1996; Rogers et al. 1998; see Lin 2007 for a brief review) data assimilation cycle adopted by

NCEP's Eta model by using 3DVAR technique.

Data types used in the 3DVAR of the ETA model are:
1. rawinsonde mass and wind
2. pibal (pilot balloon) winds
3. dropwindsondes
4. wind profilers
5. surface land temperature and moisture
6. oceanic surface data (ships and buoys)
7. aircraft winds
8. satellite cloud-drift winds
9. oceanic TOVS thickness retrievals
10. GOES and SSM/I precipitable water retrievals
11. ACARS temperature data, surface winds over land
12. VAD winds from NEXRAD
13. SSM/I oceanic surface winds
14. tropical cyclone bogus data.

The last five types of data were not included in the OI (Optimal Interpolation) technique which was replaced by 3DVAR in EDAS. Abbreviations of the data types may be found in Parrish et al. (1996) and Rogers et al. (1998).

Some more advanced techniques have been developed by using adjoint model in intermittent data assimilation systems (e.g. Zou and Kuo 1996; Pu et al. 1997; Huang 1999).

The intermittent updating process is appropriate as long as most available data are taken at a fixed time period, which may vary from 3 to 12 h in practice.

WRF 3DVAR:
http://www.mmm.ucar.edu/mm53dvar/docs/3DVARTechDoc.pdf

> ## *Continuous (Dynamic) 4DDA*
However, in order to take advantage of the asynoptic data, which come in much more frequent than the synoptic data, methods of *continuous* or *dynamic 4DDA* are desired.

In these methods, the observational data are essentially introduced into the assimilation system at each time step of the model integration during the assimilation time period.

Examples of this type of *continuous 4DDA* are
(1) *Nudging (Newtonian) relaxation* (Hoke and Anthes 1976; Kistler 1974),
(2) *Variational assimilation* or *4DVAR* (Sasaki 1969; Stephens1970; see Daley 1991 for reviews), and
(3) *Kalman-Bucy filtering* (Kalman and Bucy 1961; Ghil et al. 1981).

o ## *Nudging (Newtonian) relaxation method*
In the *nudging* or *Newtonian relaxation method*, there is preforecast integration period during which the model variables are driven toward the observations by adding extra forcing terms in the equations.

When the actual initial time is reached, the extra terms are dropped from the model equations and the forecast proceeds

without any forcing. For example, a forcing term is added to the x-momentum equation,

$$\frac{\partial u}{\partial t} = -V \cdot \nabla u + fv - \frac{1}{\rho}\frac{\partial p}{\partial x} + \frac{u - u_{obs}}{\tau}.$$
(13.3.4)

The time scale for the relaxation, τ may depends on the variable, and is chosen to slowly increase (decrease) prior to (after) the time of the observation to prevent any shocks to the model during the assimilation time period.

Nudging has been tested for use with the new generation of observing systems, such as dropwindsondes, wind profilers, and surface data.

Compared to the variational assimilation (4D-VAR) and Kalman-Bucy filtering techniques, to be discussed below, the nudging or Newtonian relaxation technique is less elegant mathematically, but is very practical.

Reference: http://www.mmm.ucar.edu/mm5/documents/mm5-desc-pdf/sec4.pdf

o *4DVAR*
In the ***variational data assimilation*** or ***4DVAR***, one tries to create the best possible fit between the model and the observational data such that the adjusted initial conditions are optimal for use in subsequent model forecasts.

For example, in Fig. 13.14 shows that the value produced by the first analysis is A (Sasaki 1969; Stephens 1970).
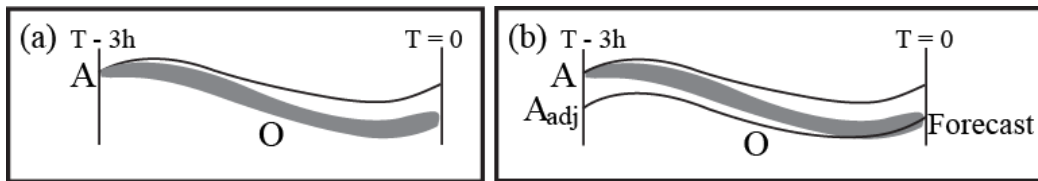
Fig. 13.14: A sketch of four-dimensional variational data assimilation (4DVAR). (a) The value produced by the first analysis is A, which fits the data well at T-3h (denoted by A), but leads to a forecast (solid line) that does not match the observations (shaded) well by T = 0 h. The shaded band is the observations. Note that even data collected at the same time do not necessarily agree with each other. (b) An iterative approach, i.e. the adjoint method, is taken to adjust the initial analysis so that it is optimal for prediction. (Courtesy of F. H. Carr)

Although it fits the data well at T-3h, it leads to a forecast that does not match the observations well by T = 0h. The band of dots is the observations. Note that even data collected at the same time do not necessarily agree with each other.

One way to resolve the problem is to take the ***adjoint method*** (Lewis and Derber 1985), as one type of the variational 4DDA or 4DVAR, in which an iterative approach is used to adjust the initial analysis so that it is optimal for prediction.

In other words, the adjusted analysis (A_{adj}) leads to a model trajectory (heavy curve) that produces a better 3-h forecast for T = 0 h, even though it may not be the best fit at T-3h.

More detailed information can be found at:
http://www.ecmwf.int/newsevents/training/rcourse_notes/DATA_ASSIMILATION/ASSIM_CONCEPTS/Assim_concepts11.html

WRFDA: http://www2.mmm.ucar.edu/wrf/users/wrfda/

o ***Kalman filtering***

In the Kalman filtering technique (Ghil et al. 1981), the data sequentially adjust the assimilated fields as the model is integrated forward in time.

The Kalman filter minimizes the analysis error variance not only at every time step, but over the entire assimilation period in which data are provided.

Through an application of Bayesian ideas in a dynamical sense (Kalman 1960; Lorenc 1986), the filter is able to extract all useful information from the observational increment or residual at each time step, thus allowing observations to be discarded as soon as they are assimilated.

One promising simplification of Kalman filtering is ensemble Kalman filtering (EnKF) (see Kalnay 2003) or http://en.wikipedia.org/wiki/Ensemble_Kalman_filter.

Evaluation of a WRF EnKF against a 3DVAR can be found at:
http://www.image.ucar.edu/pub/WRF_EnsembleFilter.pdf.

In order to involve the standard or nonstandard data to reduce or eliminate the spin-up error caused by the lack, at the initial time, of the fully developed vertical circulation required to

support regions of large rainfall rates, one may adopt the
diabatic** or **physical normal mode initialization.
This may improve quantitative precipitation forecasts,
especially early in the forecast. Two key issues may be raised
here:
(1) Choice of technique and
(2) Sources of hydrologic/hydrometeor data.

Diabatic heating information in nonlinear normal mode
initialization may be either from the model estimates or from
observed rainfall data. Rainfall data (a 2D field) has been
used to infer 3D fields of latent heating, moisture and
divergence by a number of ways:

(a) Static methods (Donner 1988; Turpeinen et al. 1990;
    Kasahara 1992; see Lin 2007),
(b) Dynamic methods (Ninomiya and Kurihara, 1987; Carr
    and Baldwin 1991; Krishnamurti et al. 1991),
(c) Adjusting the convective parameterization scheme to
    match the observed rainfall (Krishnamurti et al. 1991;
    Donner 1988; Puri and Miller 1990),
(d) Latent heat nudging (Fiorino and Warner, 1981; Wang
    and Warner, 1988; Turpeinen et al. 1990; Jones and
    Macpherson 1997).

A **major problem** in all of the above techniques is the need
for accurate vertical distribution of the heating and moistening
rates.

For example,

(i)   surface rain gauge data not available on hourly basis,
(ii)   rawinsode data is sparse horizontally (may be overcome by combining infrared and microwave satellite estimates),
(iii) cloud water and ice data to be deduced from the network of Doppler radars are not complete (retrieval techniques are critical).

The 4DVAR incorporate observed data into a mesoscale model, such as WRFDA, in a dynamically and physically consistent manner to derive improved initial conditions.

Through the model precipitation calculation and adjoint model, information from the space of the model variables, such as wind, temperature, and humidity, can be uniquely projected to that of the measured variables (i.e. rainfall rates), and back, in a consistent manner.

Some mesoscale or local analysis and prediction systems have been proposed, such as *RUC/MAPS* and *LAPS*.

The *Rapid Update Cycle* (*RUC;* see Benjamin et al. 1991, 2000) is an operational atmospheric prediction system comprising primarily of a numerical forecast model and an analysis system to initialize that model.

The *Mesoscale Analysis and Prediction System (MAPS)* is the research counterpart to the *RUC*. The RUC has been developed to serve users needing short-range weather forecasts, including those in the US aviation community.

In *MAPS*, a mesoscale model is employed to make a 3h data assimilation in $\sigma-\theta$ coordinates. It improves the analysis of upper-level frontal structures. Advances in remote sensing from earth- and space-borne systems, expanded in situ observation network, and increased low-cost computer capability allow an initialization for meso- and convective scale models.

LAPS (*Local Analysis and Prediction System*, see McGinley et al., 1992; Albers et al., 1996) uses data from local *mesonetwork* (*mesonet*) of surface observating systems, Doppler radars, satellites, wind and temperature (RASS) profilers, as well as aircraft are incorporated every hour into a three-dimensional grid covering a 1000km x 1240km area.

LAPS has analysis and prediction components. The prediction component is being configured using the SFM (modified RAMS), MM5, and ETA model. Any or all of these models, usually being initialized with LAPS analyses, is run to provide 0-18 h forecasts.

Many of the data assimilation methods developed for larger scale models cannot be applied to the stormscale models.

For example, storm-scale phenomena are highly ageostrophic and divergent, so that the constraints between the mass and momentum field applied at larger scale (geostrophic and thermal wind balances) cannot be applied to the storm scale.

Furthermore, the mass field is inferred from the reflectivity and radial velocity measured by Doppler radars, instead of being measured directly. Thus, the retrieval techniques become very critical.

As shown in Fig. 13.15, the adjoint method can improve the accuracy in retrieving the thermodynamic fields, compared to the direct integration of the continuity equation (Sun and Crook 1996).
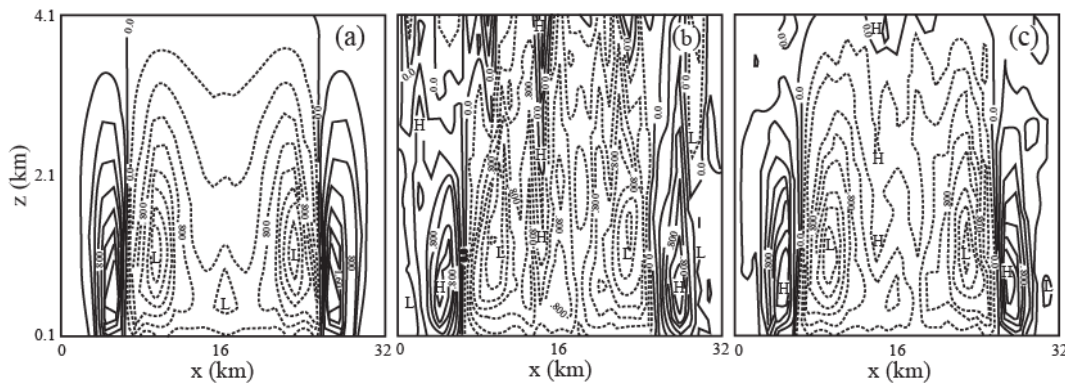
Fig. 13.15: Vertical velocity field from (a) control run, (b) vertical integration of the continuity equation, and (c) adjoint retrieval. (After Sun and Crook 1996)

13.4 Nonlinear Aliasing and Instability, and Numerical Smoothing

In discussing numerical instabilities in the previous chapter, we have neglected the nonlinear effects.

However, in the real atmosphere, kinetic energy generated at large scale or mesoscale tends to transfer to smaller scales.

When it is transferred to the so-called ***inertial subrange***, the kinetic energy is neither produced nor dissipated, but handed down to smaller and smaller scales.
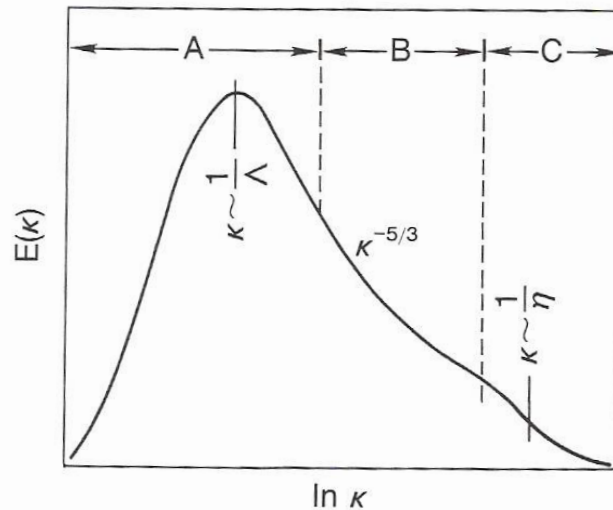
F IG. 2.1. Schematic of energy spectrum in the atmospheric boundary layer showing distinct regions of energy production (A) and dissipation (C) and the inertial subrange (B), where both energy production and dissipation are negligible. Λ is the integral scale of turbulence and η is the Kolmogorov microscale.

(From Tennekes and Lumley 1972)

(κ: wavenumber, $E(\kappa)$: energy)

(2) In the ***energy-containing range*** (Range A), which contains the bulk of the turbulenct energy and where energy is produced by buoyancy and shear.

(3) In the ***inertial subrange*** (Range B), the kinetic energy is independent of original forcing of the motion and molecular dissipation, according to $E(k)=a\varepsilon^{2/3} k^{-5/3}$,

where a is a constant, ε is the eddy dissipation rate, and k is the wave number.

In this range, <u>energy is neither produced nor dissipated but handed down (transferred) to smaller and smaller scales</u>.

(4) In the ***dissipation range*** (Range C), where KE is converted to internal energy by molecular interaction.

In a numerical mesoscale model, this cascade of energy to smaller scales cannot occur because the smallest feature that can be resolved has a wavelength of $2\Delta x$.

For example, let us consider 2 waves with the same amplitude ϕ_o and different wave numbers, k_1 and k_2,

$$\phi_1 = \phi_o \cos k_1 \Delta x , \tag{13.4.1}$$
$$\phi_2 = \phi_o \cos k_2 \Delta x .$$

A *nonlinear interaction* between these two waves produces

$$\phi_1 \phi_2 = (\phi_o^2 / 2)\left[\cos(k_1 + k_2)\Delta x + \cos(k_1 - k_2)\Delta x\right]. \tag{13.4.2}$$

For example, this may happen in the momentum equation,

$$U\frac{\partial u'}{\partial x} + u'\frac{\partial u'}{\partial x} = U\frac{\partial u'}{\partial x} + \frac{1}{2}\frac{\partial}{\partial x}(u'^2) .$$

It can be seen clearly from the above equation, two waves with wave numbers, $k_1 + k_2$ and $k_1 - k_2$ are resulted from this *wave-wave interaction*.

Assume k_1 and k_2 represent the following $2\Delta x$ and $4\Delta x$ waves,

$$k_1 = 2\pi /(2\Delta x),$$
$$k_2 = 2\pi /(4\Delta x), \qquad\qquad\qquad\qquad (13.4.3)$$

then we have

$$\phi_1 \phi_2 = \left(\frac{\phi_o^2}{2}\right)\left\{\cos\left[2\pi\Delta x\left(\frac{3}{4\Delta x}\right)\right] + \cos\left[2\pi\Delta x\left(\frac{1}{4\Delta x}\right)\right]\right\}. \qquad (13.4.4)$$

The second term inside the braces of the right hand side of the above equation is a $4\Delta x$ wave, which can be appropriately represented by the grid mesh.

However, the first term is a $1.33\Delta x$ wave, which cannot be resolved by the grid mesh. This wave will be fictitiously represented by a $4\Delta x$ wave because the first integer multiple of $4\Delta x/3$ is $4\Delta x$.

This phenomenon is called *nonlinear aliasing*.

Fig. 13.16 shows a schematic that illustrates of how a physical solution with a wavelength of $4\Delta x/3$, caused by the nonlinear interaction of $2\Delta x$ and $4\Delta x$ waves, is seen as a computational $4\Delta x$ wave in the numerical grid mesh.
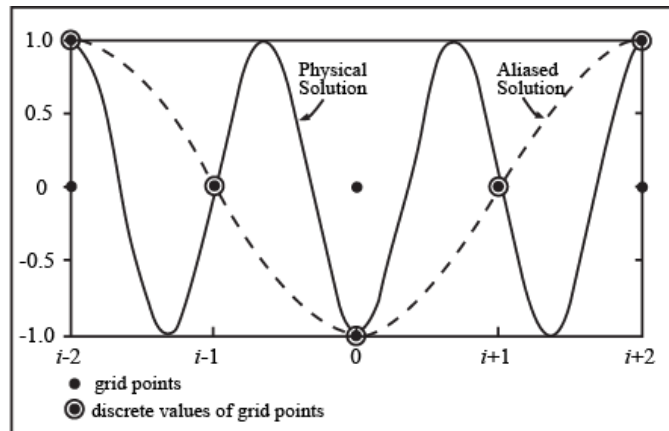
Fig. 13.16: Schematic illustration of nonlinear aliasing. A physical solution with a wavelength of $1.33\Delta x$, caused by the nonlinear interaction of waves of $2\Delta x$ and $4\Delta x$, is seen as a $4\Delta x$ wave in a numerical grid mesh. (After Pielke 2002, reproduced with permission from Elsvier.) (From Lin 2007)

In the real world, we have the large-scale disturbance generated by forcing, which then cascades to a mesoscale disturbance, small-scale disturbance, and then dissipates at an even smaller scale.

However, it does not seem to happen in the same way in the numerical model, in which waves with wavelength shorter than $2\Delta x$ will be represented as larger scale waves.

Therefore, even if a numerical method is *linearly stable*, the results can degrade into *computational noise*.

This erroneous accumulation of energy can cause the model dependent variables to increase in magnitude abruptly without bound. This phenomenon is called ***nonlinear computational instability***.

There are two methods have been proposed to avoid the nonlinear instability:

(a) proper parameterization of the subgrid-scale correction terms, such as $\overline{u'w'}$, $\overline{v'w'}$, $\overline{\theta'w'}$, etc., so that energy is extracted from the averaged equations, or

(b) use of a spatial smoother or filter to remove the shorter waves, but leaves the longer waves relatively unaffected.

The first approach is better than the second one because it is based on physical principle. However, it requires a good knowledge about the *subgrid-scale correlation* terms.

The second approach can be accomplished in a relatively easier manner, such as those proposed by Shapiro (1970; 1975).

To understand numerical smoothing, we may consider a simple one-dimensional, ***three-point operator***,

$$\overline{\phi_j} = (1-s)\phi_j + (s/2)(\phi_{j-1} + \phi_{j+1}), \tag{13.4.5}$$

where $x = j\Delta x$ and s is a constant which may be negative.

If this operator is applied to the harmonic form of a wave

$$\phi = A\,e^{ikx}, \tag{13.4.6}$$

where the wave number $k = 2\pi/L$ and A is a constant which may be a complex, then the result may be written as

$$\bar{\phi} = R\phi,$$
$$R = 1 - s(1 - \cos k\Delta x) = 1 - 2s\sin^2(\pi\Delta x/L). \tag{13.4.7}$$

In the above equation, R is referred to as the *response function*.

 (5) If $R \geq 0$, then the wave number and phase are not affected, but only the wave amplitude.
 (6) If $|R| > 1$, then the wave is amplified by the operator.
 (7) If $|R| < 1$, then the wave is damped by the operator.
 (8) If $R < 0$, then the phase of the wave is shifted by 180º, which is undesirable.
 (9) With $s = 1/2$, we obtain the *second-order smoother*,

$$\bar{\phi}_j = (1/4)(\phi_{j-1} + 2\phi_j + \phi_{j+1}), \tag{13.4.8}$$

and

$$R(1/2) = 1 - (1/2)(1 - \cos k\Delta x) = \cos^2(\pi\Delta x/L). \tag{13.4.9}$$

From above, if $L = 2\Delta x$, then $R = 0$. Hence, for a $2\Delta x$ wave, the smoother will eliminate it immediately.

Since a ***three-point smoother*** damps the shorter waves too strongly, it is less desirable.

A *five-point smoother* can be obtained by applying 2 successive three-point smoother with $s = 1/2$ and $-1/2$,

$$\overline{\overline{\phi_j}} = \frac{1}{16}\left[10\phi_j + 4\left(\phi_{j-1} + \phi_{j+1}\right) - \left(\phi_{j-2} + \phi_{j+2}\right)\right]$$
$$= \phi_j - \frac{1}{16}\left[6\phi_j - 4\left(\phi_{j-1} + \phi_{j+1}\right) + \left(\phi_{j-2} + \phi_{j+2}\right)\right] \quad\quad (13.4.10)$$

The above smoother will also remove the $2\Delta x$ wave immediately, but preserve more of the longer waves.

In fact, the above *5-point smoother* is analogous to the finite difference form of the *4th-order diffusion equation*,

$$\frac{\partial \phi}{\partial t} - c\frac{\partial^4 \phi}{\partial x^4} = 0 , \quad\quad (13.4.11)$$

which has a finite difference form,

$$\phi_j^{\tau+1} = \phi_j^{\tau} - \gamma\left[6\phi_j^{\tau} - 4(\phi_{j-1}^{\tau} + \phi_{j+1}^{\tau}) + (\phi_{j-2}^{\tau} + \phi_{j+2}^{\tau})\right], \quad\quad (13.4.12)$$

where $\gamma = c\Delta t / \Delta x^4$.

If we choose $\gamma = 1/16$, then the above equation is analogous to (13.4.10).

Thus, in applying the 5-point smoother, it has a similar effect as the 4th-order diffusion. That is why *numerical smoothing* has also been referred to as *numerical diffusion*.

In order to retain the amplitude of longer waves, the coefficient 1/16 in (13.4.10) or γ is often reduced. Testing is needed to find out the most appropriate coefficient of the numerical smoothing or diffusion.

In practice, the smoothing is not applied to the boundary points.

For the grid points adjacent to the boundaries, we may need to apply the three-point smoother or second-order diffusion, which has a form of

$$\overline{\phi_j} = \phi_j - \gamma_2\left[2\phi_j - \left(\phi_{j-1} + \phi_{j+1}\right)\right]. \tag{13.4.13}$$

In order to make (13.4.13) consistent with (13.4.12), we require

$$\gamma_2 = 4\gamma_1. \tag{13.4.14}$$

Note that *the leapfrog scheme produces a computational mode with $2\Delta t$ wave.*

To suppress this, we may apply the time smoother (Robert, 1966; Asselin, 1972)

$$\phi^{\tau+1} = \overline{\phi}^{\tau-1} + 2\Delta t(\partial\phi/\partial t)^{\tau}, \tag{13.4.15}$$

where

$$\overline{\phi}^{\tau-1} = \phi^{\tau-1} + \gamma\left(\phi^{\tau} - 2\phi^{\tau-1} + \overline{\phi}^{\tau-2}\right). \tag{13.4.16}$$

Based on numerical testing, a choice of $\gamma < 0.25$ is preferable.

13.5 Modeling a Stratified Fluid System

To elucidate how to model a stratified fluid flow system, we may consider the nonlinear, hydrostatic, incompressible flow system similar to that governed by Eqs. (2.2.12) - (2.2.16) with $V = 0$,

$$\frac{\partial u'}{\partial t} + (U + u')\frac{\partial u'}{\partial x} + v'\frac{\partial u'}{\partial y} + w'\left(U_z + \frac{\partial u'}{\partial z}\right) - fv' + \frac{1}{\rho}\frac{\partial p'}{\partial x} = \nu\nabla^2 u', \qquad (13.5.1)$$

$$\frac{\partial v'}{\partial t} + (U + u')\frac{\partial v'}{\partial x} + v'\frac{\partial v'}{\partial y} + w'\frac{\partial v'}{\partial z} + fu' + \frac{1}{\rho}\frac{\partial p'}{\partial y} = \nu\nabla^2 v', \qquad (13.5.2)$$

$$\frac{1}{\overline{\rho}}\frac{\partial p'}{\partial z} = g\frac{\theta'}{\overline{\theta}}, \qquad (13.5.3)$$

$$\frac{\partial u'}{\partial x} + \frac{\partial v'}{\partial y} + \frac{\partial w'}{\partial z} = 0, \qquad (13.5.4)$$

$$\frac{\partial \theta'}{\partial t} + (U + u')\frac{\partial \theta'}{\partial x} + v'\frac{\partial \theta'}{\partial y} + w'\left(\frac{N^2\overline{\theta}}{g} + \frac{\partial \theta'}{\partial z}\right) = \frac{\theta_o}{c_p T_o}q' + \kappa\nabla^2\theta', \qquad (13.5.5)$$

where
q' : the diabatic heating rate in $J\,kg^{-1}$ (surface and/or elevated heating),
ν : is the *molecular kinematic viscosity coefficient,*
κ : is the *molecular thermal diffusivity coefficient,* and the Brunt-Vaisala frequency N is defined as $N^2 = (g/\overline{\theta})(d\overline{\theta}/dz)$.

The basic state is assumed to be in geostrophic and hydrostatic balances.

The basic and perturbation quantities have been separated in the above system, which allows one to examine the nonlinear effects by comparing with the corresponding linear simulation.

Note that the above system has included molecular viscosity and diffusivity, which play insignificant roles in the atmosphere except in the *viscous sublayer*.

However, they can be used to implement the sponge layer on top of the physical domain to mimic the upper radiation boundary condition.

Rayleigh friction and Newtonian cooling have also been adopted to mimic the sponge layer.
The planetary boundary layer processes are normally parameterized by eddy viscosity and diffusion.

To elucidate how to simulate the nonlinear system of (13.5.1)-(13.5.5), we may consider apply the scheme of leapfrog in time and second-order centered in space to the prognostic equations to obtain $u^{\tau+1}$, $v^{\tau+1}$ and $\theta^{\tau+1}$ from other variables at time steps τ and $\tau-1$, based on (13.5.1), (13.5.2) and (13.5.5), respectively.

The vertical velocity $w^{\tau+1}$ can then be obtained by integrating the continuity equation, (13.5.4) upward.

The upper boundary condition can be approximated by a sponge layer with ν increasing from the top of the physical domain to

the top of the model domain, or following the flow chart Fig. 13.10 to apply the upper radiation boundary condition numerically.
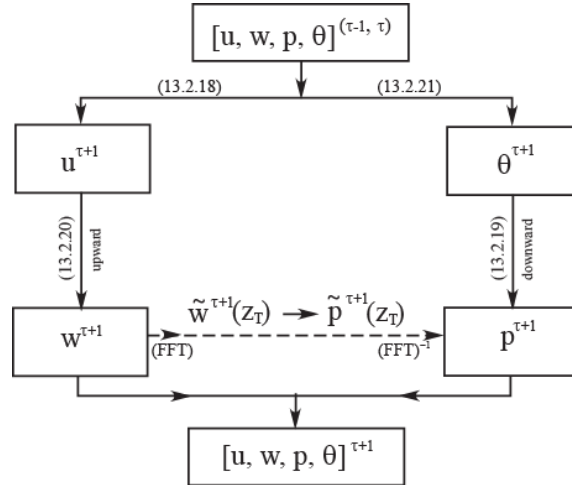

Fig. 13.10: A flow chart for modeling the fluid flow system of (13.2.18) - (13.2.21) and implementing the numerical upper radiation boundary condition at the top of computational domain. FFT and FFT^{-1} denote the Fast Fourier Transform and the inverse Fast Fourier Transform.

Following Fig. 13.10, we can obtain $p^{\tau+1}$ by integrating the hydrostatic equation (13.5.3) downward.

In this way, all variables at time step $\square+1$ are then obtained numerically. More sophisticated numerical schemes may be chosen to simulate the above system.

In some mesoscale models, the hydrostatic assumption is relaxed to more properly simulating *deep convection* and effects of steep topography. A set of fully compressible fluid system may be written as,

$$\frac{Du}{Dt} = fv - \frac{1}{\rho}\frac{\partial p}{\partial x} + \nu\nabla^2 u,$$

(13.5.6)

$$\frac{Dv}{Dt} = -fu - \frac{1}{\rho}\frac{\partial p}{\partial y} + \nu\nabla^2 v,$$

(13.5.7)

$$\frac{Dw}{Dt} = -\frac{1}{\rho}\frac{\partial p}{\partial z} - g + \nu\nabla^2 w,$$

(13.5.8)

$$\frac{D\theta}{Dt} = S_\theta + \kappa\nabla^2\theta$$

(13.5.9)

$$\frac{D\phi}{Dt} = S_\phi + \kappa\nabla^2\phi, \quad \phi = q_v, q_c, q_i, q_r, q_s, q_g,$$

(13.5.10)

$$\frac{D\rho}{Dt} + \rho\nabla\cdot V = 0,$$

(13.5.11)

$$p = \rho R T,$$

(13.5.12)

$$\theta = T_v\left(\frac{p_o}{p}\right)^{R_d/c_p},$$

(13.5.13)

$$T_v = T(1 + 0.61q_v),$$

(13.5.14)

where

T_v is called *virtual temperature,*

θ is the *virtual potential temperature* (with subscript *v* dropped),

p_o is the basic state pressure at the ground, usually taken as 1000 hPa,

S_θ is any source or sink of θ, such as surface long-wave radiation and elevated latent heating,

S_ϕ is any source or sink of the hydrometeor ϕ, such as *water vapor* (q_v), *cloud water* (q_c) , *rain* (q_r), *cloud ice* (q_i), *snow* (q_s), *graupel/hail* (q_g).

The virtual temperature is the temperature a dry air parcel would have if its pressure and density were equal to those of a given sample of moist air.

The virtual temperature is a fictitious temperature of a moist air parcel that satisfies the equation of state for dry air.

As mentioned above, terms with ν and $\square$ in the above equations represent molecular viscosity and thermal diffusion effects, which play insignificant role in atmospheric motions and processes except in the *viscous sublayer*.

The viscous sublayer only occupies a few centimeters above the earth's surface, thus is often ignored in mesoscale models.

As will be discussed in the next chapter, the subgrid turbulent flux terms will come into play when the unresolved subgrid turbulent mixing is considered.

The above equations may also be represented in terms of the *Exner funtion*, to be defined below.

Following Tapp and White (1976) and Klemp and Wilhelmson (1978), the governing equations of a fully compressible fluid system may be derived.

Including the moisture, the equation of state may be written in the form,

$$p = \rho R_d T_v,$$ (13.5.15)

where q_v is the *mixing ratio* of *water vapor*.

In order to avoid an explicit treatment of the density, an **Exner function** has been adopted in some mesoscale and cloud-scale models,

$$\pi = c_p \left(\frac{p}{p_o} \right)^{R_d/c_p} = \frac{c_p T_v}{\theta_v} . \tag{13.5.16}$$

The pressure gradient force terms can then be approximately represented by

$$\frac{1}{\rho} \frac{\partial p}{\partial x_i} = \theta_{vo} \frac{\partial \pi}{\partial x_i}, \quad i = 1, 2, 3, \tag{13.5.17}$$

where

θ_{vo} is the initial undisturbed state θ_v and a function of z only, defined as $\theta_v = \theta_{vo} + \theta_{v1}$.

The Exner function may be partitioned into $\pi = \pi_o + \pi_1$, where π_o is the initial basic state and π_1 is the perturbation from the initial state π_o.

The initial basic state is assumed to be in geostrophic balance in horizontal and hydrostatic balance in vertical,

$$\frac{\partial \pi_o}{\partial x} = f v_g; \quad \frac{\partial \pi_o}{\partial y} = -f u_g, \tag{13.5.18}$$

$$\frac{\partial \pi_o}{\partial z} = -\frac{g}{\theta_{vo}}, \tag{13.5.19}$$

The advantages of using π, instead of p are that (Pielke 2002):

(a) ρ is not treated explicitly in the governing equations,

(b) π does not present in the buoyancy term even if the vertical scale of the motion or disturbance L_z is equivalent to the scale height H;

(c)   There is no need to compute the density perturbation;

(d)   Less truncation error is introduced since $\partial \pi_o / \partial z$ is much less than $\partial p_o / \partial z$.

One disadvantage of using the Exner function is that the anelastic equation for π is much more complicated, such as that used in Clark (1977), and need a Poisson equation solver.

In the terrain-following coordinates, coding of the Poisson equation solver becomes very complicated (Chen 1991; Huang 2000).

Thus, the momentum equations can then be derived by using the Exner function and approximating θ_v by θ_{vo} in pressure gradient forces, we have

$$\frac{Du}{Dt} = f(v - v_g) - \theta_{vo}\frac{\partial \pi_1}{\partial x} + \nu\nabla^2 u,$$
(13.5.20)

$$\frac{Dv}{Dt} = -f(u - u_g) - \theta_{vo}\frac{\partial \pi_1}{\partial y} + \nu\nabla^2 v,$$
(13.5.21)

$$\frac{Dw}{Dt} = -\theta_{vo}\frac{\partial \pi_1}{\partial z} + g\left[\frac{\theta_{v1}}{\theta_{vo}} - q_H\right] + \nu\nabla^2 w,$$
(13.5.22)

$$q_H = q_c + q_i + q_r + q_s + q_g$$

where

$D/Dt \equiv \partial/\partial t + u\partial/\partial x + v\partial/\partial y + w\partial/\partial z$, subscripts o and 1 denotes the initial basic state and perturbation of a variable, respectively, and q_c, q_i, q_r, q_s, and q_g denote the mixing ratios of cloud water, cloud ice, rainwater, snow, and graupel/hail, respectively.

The pressure equation can be written as

$$\frac{D\pi_1}{Dt} = -\frac{1}{\theta_{vo}}(\mathbf{V} \cdot \nabla \pi_o) - \left(\frac{R_d \pi_o}{c_v \rho_o \theta_{vo}^2}\right)\nabla \cdot (\rho_o \theta_{vo} \mathbf{V}) - \left(\frac{R_d \pi_1}{c_v}\right)\nabla \cdot \mathbf{V}$$
$$+ \frac{R_d(\pi_o + \pi_1)}{c_v \theta_v}\dot{\theta} + \kappa\nabla^2 \pi_1,$$

$$(13.5.23)$$

where $\dot{\theta} \equiv D\theta/Dt$ represents the diabatic heating per unit mass ($J\ kg^{-1}$).

The thermodynamic equation and equations governing hydrometeors may be written as

$$\frac{D\theta}{Dt} = S_\theta + \kappa\nabla^2 \theta,$$

$$(13.5.24)$$

$$\frac{D\phi}{Dt} = S_\phi + \kappa\nabla^2 \phi, \qquad \phi = q_v,\ q_c,\ q_i,\ q_r,\ q_s,\ q_g,$$

$$(13.5.25)$$

where S terms denote the source and sink of the variable, which represent microphysical processes.

The advantage of using the fully-compressible fluid system of (13.5.20)-(13.5.25) is that every equation can be integrated alone numerically to obtain its own value at the next time step, without having to couple with other equations, such as the hydrostatic, incompressible fluid system of (13.5.1)-(13.5.5).

However, this set of equations contains **_sound waves_**, which propagate at much larger speeds than the gravity waves and require a very small time step to insure the numerical stability.

In practice, it is almost impossible to adopt such a small time step, even at the research mode of numerical simulations.

In order to improve numerical efficiency of the above atmospheric fluid system, Klemp and Wilhelmson (1978) proposed a ***time-splitting scheme***, which was originally proposed by Marchuk (1974).

In the time-splitting scheme, equations with no sound wave modes, i.e. (13.5.24) and (13.5.25), embedded are marched with a large time step, Δt , while equations with sound waves embedded, i.e. (13.5.20)-(13.5.23), are integrated with a small time step $\Delta \tau$ from time $t - \Delta t$ to $t + \Delta t$.

To insure numerical stability, a semi-implicit method have been used in vertical for the small-time-step integration.

Browning and Kreiss (1994) argued that the *Klemp-Wilhelmson splitting scheme is weakly unstable for symmetric hyperbolic systems* and it is necessary to add an ad hoc dissipation operator to control the instability.

They also suggested that for badly skewed systems, Klemp-Wilhelmson splitting scheme, in which semi-implicit method is applied in vertical, also excites high-frequency waves.

Therefore, they proposed the leapfrog method for the multiscale system for the atmospheric modeling (Browning and Kreiss 1986).

On the other hand, Skamarock and Klemp (1994) showed that the Klemp-Wilhelmson time splitting scheme is efficient and reasonably accurate as compared to other models using a single small time step to integrate the fully compressible fluid system.

Based on scale analysis, Ogura and Philips (1962) found that the only important term in (13.5.23)

$$\frac{D\pi_1}{Dt} = -\frac{1}{\theta_{vo}}(V \cdot \nabla \pi_o) - \left(\frac{R_d \pi_o}{c_v \rho_o \theta_{vo}^2}\right) \nabla \cdot (\rho_o \theta_{vo} V) - \left(\frac{R_d \pi_1}{c_v}\right) \nabla \cdot V$$
$$+ \frac{R_d(\pi_o + \pi_1)}{c_v \theta_v} \dot{\theta} + \kappa \nabla^2 \pi_1,$$

(13.5.23)

for representing convection is the second term on the right hand side, which may be approximated by the anelastic continuity equation,

$$\nabla \cdot (\rho_o V) = 0 .$$

(13.5.26)

Taking the time derivative of the above equation and using the momentum equations yields an elliptic equation, the above equation may be rewritten

$$\nabla^2 \theta_{vo} \pi_1 + \nabla \theta_{vo} \cdot \nabla \pi_1 + \frac{\partial}{\partial z}(\ln \rho_o) \theta_{vo} \frac{\partial \pi_1}{\partial z} = source\ terms ,$$

(13.5.27)

where the source terms include acceleration terms (e.g. see Huang 2000).

As discussed in Chapter 2, the anelastic approximation may be further improved by adopting the pseudo-incompressible approximation (Durran 1989).

One of the disadvantages in adopting the anelastic approximation is that (13.5.27) becomes very complicated when it is transformed into a terrain-following coordinates, which also makes the computations expensive.

13.6 Predictability and Ensemble Forecasting

Basically, *numerical weather prediction* uses numerical methods to approximate a set of partially differential equations, which govern the weather systems, on discrete grid points in a finite domain to predict the weather systems and processes for a certain time in the future.

In order to numerically integrate these partial differential equations with time, one needs to start the integration at certain time for the finite domain.

As mentioned earlier, mathematically this corresponds to solving an *initial-value and boundary-value problem*.

Thus, in a numerical weather prediction model, the meteorological variables need to be specified at the initial time, i.e. the *initial conditions*, and at the boundaries of the domain, i.e. *boundary conditions*.

In earlier part of this Chapter, we have discussed about various ways in implementing the initial and boundary conditions for a mesoscale model, which are also applicable to a numerical weather prediction model.

The accuracy of a numerical weather prediction model thus depends on the accuracies of the initial conditions and boundary conditions.

The *major problems* we are facing in the numerical weather prediction today is the *lack of sufficient and accurate initial conditions*, as well as *more accurate and sufficient boundary conditions* and appropriate ways to implement them at the lateral boundaries of a finite domain of interest.

One example is that we do not have enough observed data in the upper air, over the ocean and polar regions. Some unconventional data, such as those retrieved from radar and satellite observations, have been used to help supply the data in data-void regions.

Improvement of global numerical weather prediction models is also important in improving the accuracy of the regional numerical weather prediction model since the former are often used to provide the initial and boundary conditions for the latter.

The *inaccuracy of numerical weather prediction* may also come from the numerical approximation of the partial differential equations governing atmospheric motions on the discrete points of a model domain, and the representation of the weather phenomena and processes occurred within grid points of a numerical model, i.e. the parameterization of subgrid-scale weather phenomena and processes.

The accuracy of a numerical method can be improved by

(1) adopting a higher-order approximation of the partial differential equations used in the numerical weather prediction models, as well as

(2) using a more accurate, but stable approximation methods.

These require an increase of computing power as well as a better understanding of numerical approximation methods.

The accuracy of subgrid-scale parameterizations can be improved by

(1) reducing the grid interval of a numerical weather prediction model, as well as
(2) a better understanding of the weather phenomena and processes, which will be discussed in the next Chapter.

Another challenge of numerical weather prediction is whether the weather systems are predictable or not.

If they are intrinsically unpredictable, then the improvements in more accurate initial and boundary conditions, numerical methods, and subgrid-scale parameterizations of a numerical weather prediction will have their limitations.

In reality, the weather systems are considered to have ***limited predictability***.

Thus, it leaves us some room to make improvements of the accuracy of numerical weather prediction models.

13.6.1 Predictability problem

In 1919, Bjerknes stated that

> "*if the initial conditions of the atmosphere were known with sufficient accuracy, and if the equations by which the motions of the atmosphere and the physical changes taking place therein were also known with sufficient accuracy, then the state of the atmosphere could be determined completely by some super-mathematician at any subsequent time.*" (Quoted in Schumann 1950)

Schumann is one of the earliest that concerned about the uncertainties in the subjective forecasts.

In early 1950s, some meteorologists started to apply statistical methods to weather prediction to cope with the uncertainties encountered in forecasting (Gleeson 1961). The weather forecasting problem has been viewed as evolving probabilities.

It has been realized that even with improved model techniques, the weather prediction has its own inherit limitations due to the inevitable model deficiencies and errors in the initial conditions, or the ***predictability problem***.

In his pioneering work of *dynamical system*, Lorenz (1963) discovered some fundamental aspects of ***atmospheric predictability***.

He demonstrated that the atmosphere, like any dynamical system with instabilities, has an inherit time limit of *predictability*.

Based on the convective equations of Saltzman's (1962), Lorentz found that two complete different solutions were predicted by the same model with slightly different initial conditions.
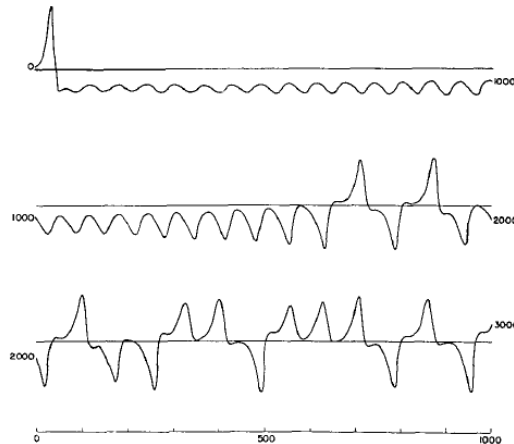

FIG. 1. Numerical solution of the convection equations. Graph of Y as a function of time for the first 1000 iterations (upper curve), second 1000 iterations (middle curve), and third 1000 iterations (lower curve).
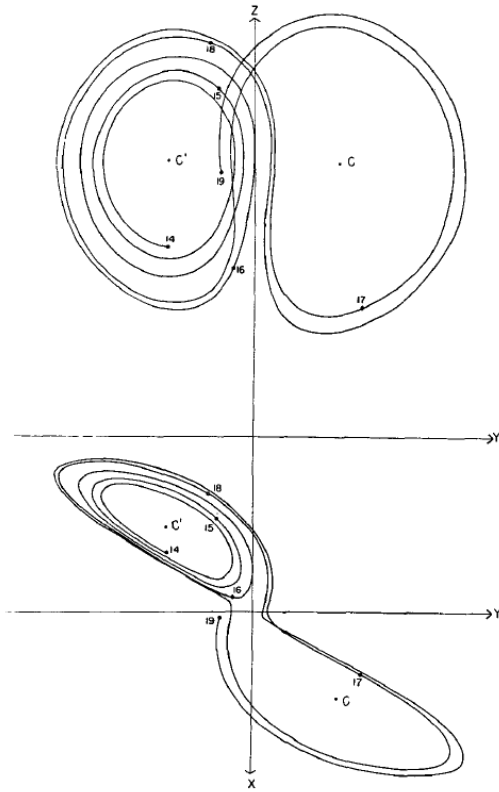
(From Lorenz JAS 1963)

FIG. 2. Numerical solution of the convection equations. Projections on the X-Y-plane and the Y-Z-plane in phase space of the segment of the trajectory extending from iteration 1400 to iteration 1900. Numerals "14," "15," etc., denote positions at iterations 1400, 1500, etc. States of steady convection are denoted by C and C'.

He later found that errors of different spatial scales grow at different rates (Lorenz 1969a). On average, the fastest error growth occurs at small scales.

In an early predictability experiment with a general circulation model, Charney et al. (1966) found that the doubling time of root-mean-square (rms) temperature errors to be about 5 days.

This leads to an estimate of 3 weeks as the ultimate limit to atmospheric predictability and encouraged the planning and execution of the Global Atmospheric Research

Program (GARP) and the First GARP Global Experiment (FGGE) (Anthes 1986).

Lorenz (1969a) calculated that the average limit to atmospheric predictability at planetary scales is on the order of 10 days.

Using the European Centre for Medium Range Weather Forecast (ECMWF) operational model, Lorenz (1984) estimated upper and lower bounds to the predictability of 500 mb heights.

Predictability studies of large-scale motions indicate that predictability varies with horizontal scale, seasons, latitude, and synoptic pattern.

On the average, differences in the initial conditions of global numerical weather prediction models double in about 2 to 5 days, leading to estimates of the limits to atmospheric predictability of about 2 weeks.

This growth of initial differences or errors is a consequence of the nonlinear transfer of energy among different scales of motion and the presence of atmospheric instabilities.

A study of mesoscale predictability by Anthes (1986) indicated that, in at least some cases, small errors or differences in the initial conditions do not grow over a 72 hour period when the lateral boundary conditions are kept same.

These results might imply that improved meso-α scale or regional-scale numerical weather predictions are possible in the 72 hour period, provided that large-scale conditions are well forecast and that realistic surface forcing and physical parameterizations are included in high-resolution models.

Considerable efforts are needed to verify these results in future studies, especially in considering the resolution of the numerical weather prediction model is getting smaller and smaller, and data from local mesonetworks have been integrated into a very high-resolution gridded framework (e.g. Local Area Analysis and Prediction System - LAPS, see Albers et al. 1996).   (4/26/12)

13.6.2 *Ensemble* Forecast

An *ensemble forecast* is a collection of two or more forecasts that verify at the same time, which start from different initial conditions and/or are based on different forecasting procedures.

The various forecasts all represent possibilities given the uncertainties associated with forecasting.

From these possibilities, one can estimate probabilities of various events as well as an averaged or consensus forecast.

An ensemble of forecasts can be used to (Sivillo et al. 1997):

(a) Composite into a single forecast by means of a weighted average,
(b) Suggest possibilities whose probabilities can be estimated (e.g., probability of precipitation (PoP); how to make PoP?),
(c) Estimate the reliability of the composite forecast, and
(d) Suggest where additional special observations might be targeted to improve forecast accuracy.

Current ensemble forecasting at both NCEP and ECMWF is focused on the consequences of initial value errors. Both centers are generating an ensemble of forecasts by starting a forecast model from a variety of initial conditions.

Krishnamurti et al. (2001) showed that a real-time *multianalysis-multimodel superensemble forecasts* made a significant improvement in rainfall forecasts.

As indicated in Fig. 13.17, during the training period, the observed fields provide statistics that are then passed on to the area on the right, where $t > 0$.
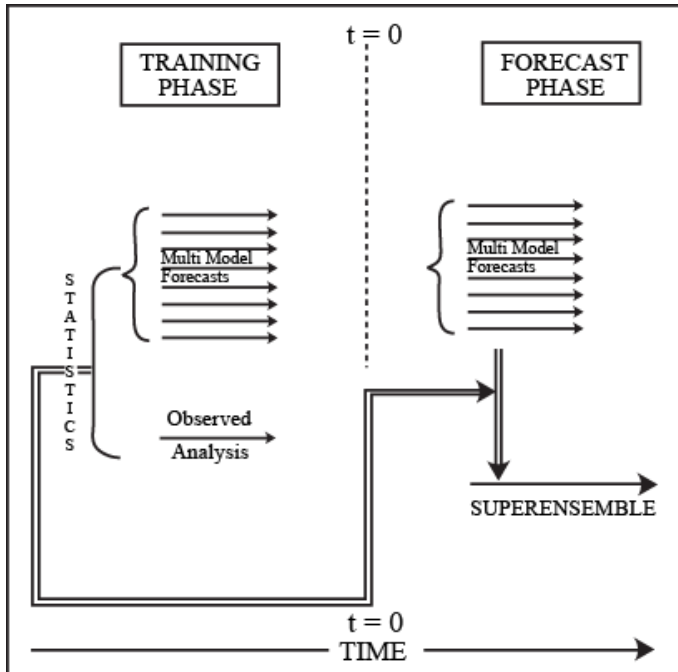
Fig. 13.17: A flow chart of multianalysis-multimodel superensemble forecasting. The vertical line in the center denotes the initial time ($t = 0$), and the area to the left denotes the training period where a large number of forecast experiments are carried out by the multianalysis-multimodel system. During the training period, the observed fields provide statistics that are then passed on to the period on the right, where $t > 0$. Here the multianalysis-mulimodel forecasts along with the statistics provide the superensemble forecasts. (Adapted after Krishnamurti et al. 2001)

The ***multianalysis-multimodel*** forecasts along with the aforementioned statistics provide the ***superensemble forecasts***.

The superensemble has a higher skill compared to that of the ensemble mean because the superensemble is selective in assigning weights and the past history of performance of models from the past statistics.

References

Albers, S., J. McGinley, D. Birkenheuer, and J. Smart, 1996: The Local Analysis and Prediction System (LAPS): Analyses of clouds, precipitation, and temperature. Wea. Forecasting, 3, 273-287.

Anthes, R. A., 1986: The general question of predictability. *Mesoscale Meteorology and Forecasting*, P. S. Ray (Ed.), Amer. Meteor. Soc., 636-656.

Anthes, R. A., and T. T. Warner, 1978: Development of hydrostatic models suitable for air pollution and other mesometeorological studies. Mon. Wea. Rev., 106, 1045-1078.

Arakawa, A., and V. R. Lamb, 1977: Computational design of the basic dynamical processes of the UCLA general circulation model. Methods in Compu. Phys., 17, Academic Press, 174-265, 337pp.

Asselin, R. A., 1972: Frequency filter for time integration. Mon. Wea. Rev., 100, 487-490.

Bacon, D. P., N. N. Ahmad, Z. Boybeyi, T. J. Dunn, M. S. Hall, P. C. S. Lee, R. A. Sarma, M. D. Turner, K. T. Waight III, S. H. Young, and J. W. Zack, 2000: A dynamically adapting weather and dispersion model: The operational multiscale environment model with grid adaptivity (OMEGA). Mon. Wea. Rev., 128, 2044-2076.

Baer, F., 1977: Adjustment of initial conditions required to suppress gravity oscillations in nonlinear flows. Contri. Atmos. Phys., 50, 350-366.

Baines, M. J., and A. J. Wathen, 1988: Moving finite element methods for evolutionary problems. I: Theory. J. Compu. Phys., 79, 245-269.

Benjamin, S. G., K. A. Brewster, R. L. Brummer, B. F. Jewett, T. W. Schlatter, T. L. Smith, and P. A. Stamus, 1991: An isentropic three-hourly data assimilation system using ACARS aircraft observations. Mon. Wea. Rev., 119, 888-906.

Benjamin, S.G., G.A. Grell, J.M. Brown, K.J. Brundage, D. Devenyi, D. Kim, B. Schwartz, T.G. Smirnova, T.L. Smith, S.S. Weygandt, and G.A. Manikin, 2000: The 20-km version of the Rapid Update Cycle. Preprints, 9th Conf. on Aviation, Range, and Aerospace Meteorology, AMS, Orlando, 421-423.

Berger, M., and J. Oliger, 1984: Adaptive mesh refinement for hyperbolic partial differential equations. J. Compu. Phys., 53, 484-512.

Bougeault, P., 1983: A non-reflective upper boundary condition for limited-height hydrostatic models. Mon. Wea. Rev., 111, 420-429.

Browning, G. L., and H.-O. Kreiss, 1986: Scaling and computation of smooth atmospheric motions. Tellus, 38A, 295-313.

Browning, G. L., and H.-O. Kreiss, 1994: Splitting methods for problems with different timescales. Mon. Wea. Rev., 122, 2614-2622.

Carr, F.H. and M. Baldwin, 1991: Assimilation of observed precipitation data using NMC's Eta Model. Preprints, AMS Ninth Conference on Numerical Weather Prediction, Denver, CO, 422-425.

Charney, J. G., R. G. Fleagle, V. E. Lally, H. Riehl, and D. Q. Wark, 1966: The feasibility of a global observation and analysis experiment. Bull. Amer. Meteor. Soc., 47, 200-220.

Chen, C., 1991: A nested grid, nonhydrostatic, elastic model using a terrain-following coordinate transformation: The radiative-nesting boundary conditions. Mon. Wea. Rev., 119, 2852-2869.

Clark, T. L., 1977: A small scale numerical model using a terrain following coordinate system. J. Compu. Phys., 24, 186-215.

Collins, W. G., and L. S. Gandin, 1990: Comprehensive hydrostatic quality control at the National Meteorological Center. Mon. Wea. Rev., 118, 2752-2767.

Crook, N. A., and J. Sun, 2000: Retrieval of thermodynamic fields with the adjoint method and comparison with the traditional technique of Gal-Chen and Hane.

Daley, R., 1991: Atmospheric Datat Analysis. Cambridge University Press, 457 pp.

Davies, H., 1976: A lateral boundary formulation for multi-level prediction models. Quart. J. Roy. Meteor. Soc., 102, 405-418.

Davies, H., 1983: Limitations of some common lateral boundary conditions used in regional NWP models. Mon. Wea. Rev., 111, 1002-1012.

Derber, J. C., D. F. Parrish, and S. J. Lord, 1991: The new global operational analysis system at the National Meteorological Center. Wea. Forecasting, 6, 538-547.

Dietachmayer, G. S., and K. K. Droegemeier, 1992: Application of continuous dynamic grid adaption techniques to meteorological modeling. Part I: Basic formulation and accuracy. Mon. Wea. Rev., 120, 1675-1706.

Dietachmayer, G. S., and K. K. Droegemeier, 1992: Application of continuous dynamic grid adaption techniques to meteorological modeling. Part II: Efficiency. Mon. Wea. Rev., 120, 1675-1706.

Donner, 1988: static and adjsting CP methods for assimilating rainfall data.???

Doswell, C. A. III, 1984: A kinematic analysis of frontogenesis associated with a nondivergent vortex. J. Atmos. Sci., 41, 1242-1248.

Doyle, J. D., D. R. Durran, C. Chen, B. A. Colle, M. Georgelin, V. Grubisic, W. R. Hsu, C. Y. Huang, D. Landau, Y.-L. Lin, G. S. Poulos, W.-Y. Sun, D. B. Weber, M. G. Wurtele, and M. Xue, 2000: An intercomparison of model-predicted wave breaking for the 11 January 1972 Boulder windstorm. Mon. Wea. Rev., 128, 901-914.

Durran, D. R., 1989: Improving the anelastic approximation. J. Atmos. Sci., **46**, 1453-1461.

Eliassen, A., and E. Palm, 1960: On the transfer of energy in stationary mountain waves. Geophy. Publ., 22, 1-23.

Fiorino and Warner 1981: nudging rainfall

Gandin, L. S., 1988: Complex quality control of meteorological observations. Mon. Wea. Rev., 116, 1137-1156.

Ghil, M., S. Cohn, J. Tavantzis, K. Bube, and E. Issacson, 1981: Applications of estimation theory to numerical weather prediction. *Dynamic Meteorology: Data Assimilation Methods*. L. Bengtsson, M. Ghil, and E. Kallen (Eds.), Springer-Verlag, 139-224.

Gleeson, T. A., 1961: A statistical theory of meteorological measurements and predictions. J. Meteor., 18, 192-198.

Haltiner, G. J., and R. T. Williams, 1980: *Numerical Prediction and Dynamic Meteorology*. 2nd ed., John Wiley & Sons, Inc., 477pp.

Harms, D. E., S. Raman, and R. V. Madala, 1992: An examination of four-dimensional data-assimilation techniques for numerical weather prediction. Bull. Amer. Meteor. Soc., 73, 425-440.

Hoke, J. E., and R. A. Anthes, 1976: The initialization of numerical models by a dynamical initialization technique. Mon. Wea. Rev., 104, 1551-1556.

Huang, C.-Y., 2000: A forward-in-time anelastic nonhydrostatic model in a terrain-following coordinate. Mon. Wea. Rev., 128, 2108-2134.

Huang, X.-Y. 1999: A generalization of using an adjoint model in intermittent data assimilation systems. Mon. Wea. Rev., 127, 766-787.

Israeli, M., and S. Orzag, 1981: Approximation of radiation boundary conditions. J. Compu. Phys., 41, 115-135.

Johnson, I. W., A. J. Wathen, and M. J. Baines, 1988: Moving finite element methods for evolutionary problems. II: Applications. J. Compu. Phys., 79, 270-297.

Jones and Macpherson 1997: latent heat nudging

Kaimal, J. C., and J. J. Finnigan, 1994: *Atmospheric Boundary Layer Flows: Their Structure and Measurement.* Oxford University Press. 289pp.

Kalman, R. E., 1960: A new approach to linear filtering and prediction problems. Trans. ASME, J. Basic Eng., 82D, 35-45.

Kalman, R. E., and R. S. Bucy, 1961: New results in linear filtering and prediction theory. Trans. ASME. J. Basic Eng., 83D, 95-108.

Kalnay. E., 2002: Atmospheric Modeling, Data Assimilation and Prediction, Cambridge University Press.

Kasahara 1992: static method for assimilating rainfall data.

Kistler, R. E., 1974: A study of data assimilation techniques in an autobarotropic primitive equation channel model. M.S. thesis, The Penn. State University, 84pp.

Klemp, J. B., and D. R. Durran, 1983: An upper boundary condition permitting internal gravity wave radiation in numerical mesoscale models. Mon. Wea. Rev., 111, 430-444.

Klemp, J. B., and D. K. Lilly, 1978: Numerical simulation of hydrostatic mountain waves. J. Atmos. Sci., 35, 78-107.

Klemp, J. B., and R. B. Wilhelmson, 1978: The simulation of three-dimensional convective storm dynamics. J. Atmos. Sci., 35, 1070-1096.

Krishnamurti, T. N., J. Xue, H. S. Bedi, K. Ingles, and D. Oosterhof, 1991: Physical initialization for numerical weather prediction over the tropics. Tellus, 43AB, 53-81.

Krishnamurti, T. N., S. Surendran, D. W. Shin, R. J. Correa-Torres, T. S. V. V. Kumar, E. Williford, C. Kummerow, R. F. Adler, J. Simpson, R. Kakar, W. S. Olson, and F. J. Turk, 2001: Real-time multianalysis-multimodel superensemble forecasts of precipitation using TRMM and SSM/I products. Mon. Wea. Rev., 129, 2861-2883.

Kuo, Y.-H., and Y.-R. Guo, 1989: Dynamic initialization using observations from a network of profilers. Mon. Wea. Rev., 117, 1975-1998.

Lewis, J. M., and J. C. Derber, 1985: The use of adjoint equations to solve a variational adjustment problem with advective constraints. Tellus, 37A, 309-322.

Lilly, D. K., 1961: A proposed staggered-grid system for numerical integration of dynamic equations. Mon. Wea. Rev., 89, 59-65.

Lin, Y.-L., 2007: *Mesoscale Dynamics*. Cambridge University Press, 630pp.

Lin, Y.-L., and T.-A. Wang, 1996: Flow regimes and transient dynamics of two-dimensional stratified flow over an isolated mountain ridge. J. Atmos. Sci., 53, 139-158.

Lin, Y.-L., R. D. Farley, and H. D. Orville, 1983: Bulk parameterization of the snow field in a cloud model. J. Clim. Appl. Meteor., 22, 1065-1092.

Long, R. R., 1953: Some aspects of stratified fluids. I. A theoretical investigation. Tellus, 5, 42-58.

Lorenc, A. C., 1986: Analysis methods for numerical weather prediction. Quart. J. Roy. Meteor. Soc., 112, 1177-1194.

Lorenc, A. C., and O. Hammon, 1988: Objective quality control of observations using Bayesian methods. Theory, and a practical implementation. Quar. J. Roy. Meteor. Soc., 114, 515-543.

Lorenz, E. N., 1963: Deterministic non-periodic flow. J. Atmos. Sci., 20, 130-141.

Lorenz, E. N. 1969a: The predictability of a flow which possesses many scales of motion. Tellus, 21, 289-307.

Lorenz, E. N., 1969b: Atmospheric predictability as revealed naturally occurring analogues. J. Atmos. Sci., 26, 636-646.

Lorenz, E. N., 1984: Estimates of atmospheric predictability at medium range. In Predictability of Fluid Motion (La Jolla Institute-1983). G. Holloway and B. J. West (Eds.), Amer. Inst. Phys., New York, 133-139.

Machenhauer, B., 1977: On the dynamics of gravity oscillations in a shallow water model, with application to normal mode initialization. Contri. Atmos. Phys., 50, 253-271.

Mahrer, Y., and R. A. Pielke, 1978: A test of an upstream spline interpolation technique for the advecgive terms in a numerical model. Mon. Wea. Rev., 106, 818-830.

McGinley, J., S. Albers and P. Stamus, 1992: Local Data Assimilation and Analysis for Nowcasting, Adv. Space Res., 12,No 7, 179-188.

Mesinger, F., and A. Arakawa, 1976: Numerical methods used in atmospheric models. Vol. 1, GARP Publ. Ser., 17, WMO/ICSU, 64 pp.

Mesinger, F., and Z. I. Janic', 1985: Problems and numerical methods of the incorporation of mountains in atmospheric models. Large-Scale Computations in Fluid Mechanics. Part 2. Lect. Appl. Meth., Vol. 33, Amer. Math. Soc., 81-120. [P. O. Box 6248, Providence, RI 02940]

Mesinger, F., Z. I. Janjic, S. Nickovic, D. Gavrilov, and D. G. Deaven, 1988: The step-mountain coordinate: model description and performance for cases of Alpine lee cyclogenesis and for a case of an Appalachian redevelopment. Mon. Wea. Rev., 116, 1493-1518.

Marchuk, G. I., 1974: *Numerical Methods in Weather Prediction*. Academic Press, 277 pp.

Miyakoda, K., and R. Moyer, 1968: A method of initialization for dynamical weather forecasting. Tellus, 20, 115-128.

Ninomiya and Kurihara 1987: dynamic method for assimilating rainfall.???

Orlanski, I., 1976: A simple boundary condition for unbounded hyperbolic flows. J. Compu. Phys., 21, 251-269.

Oliger, J., and A. Sundström, 1978: Theoretical and practical aspects of some initial boundary value problems in fluid dynamics. Int'l J. Numer. Methods Fluids, 21, 183-204.

Parrish, D. F., and J. C. Derber, 1992: The National Meteorological Center's Global spectral statistical interpolation analysis system. Mon. Wea. Rev., 120, 1747-1763.

Parrish, D. F., J. Purser, E. Rogers, and Y. Lin, 1996: The regional 3d-variational analysis for the Eta model. Preprints, 11th AMS Conf. on Num. Wea. Pred., Norfolk, VA, 19-23 August 1996.

Puri and Miller 1990: adjusting method for assimilating rainfall. ???

Perkey, D. J., and C. W. Kreitzberg, 1976: A time-dependent lateral boundary scheme for limite-area primitive equation models. Mon. Wea. Rev., 104, 744-755.

Pielke, R. A., 1974: A comparison of three-dimensional and two-dimensional numerical predictions of sea breeze. J. Atmos. Sci., 31, 1577-1585.

Pielke, R. A., 2002: *Mesoscale Meteorological Modeling.* 2nd ed., Academic Press, Inc., 676pp.

Phillips, N. A., 1957: A coordinate system having some special advantages for numerical forecasting. J. Meteor., 14, 184-185.

Pu, Z.-X., E. Kalnay, and J. G. Sela, 1997: Sensitivity forecast errors to initial conditions with a quasi-inverse linear method. Mon. Wea. Rev., 125, 2479-2503.

Ramamurthy, M. K., and F. H. Carr, 1987: Four-dimensional data assimilation in the monsoon region. Part I: Experiments with wind data. Mon. Wea. Rev., 115, 1678-1706.

Robert, A. J., 1966: The integration of a low order spectral form of the primitive meteorological equation. J. Meteor. Soc. Japan, Ser. 2, 44, 237-245.

Rogers, E., M. Baldwin, T. Black, K. Brill, F. Chen, C. DiMego, J. Gerrity, G. Manikin, F. Mesinger, K. Mitchell, D. Parrish, and Q. Zhao, 1998: Changes to the NCEP operational "early" Eta analysis/forecast system. NWS Tech. Proc. Bull., Series No. 447, Office of Meteorology, NWS, NOAA, 10pp. (http://www.nws.noaa.gov/om/tpb/447.htm.)

Saltzman, B., 1962: Finite amplitude free convection as an initial value problem - I, J. Atmos. Sci., 19, 329-341.

Sasaki, Y., 1969: Proposed inclusion of time variation terms.

Sasaki, Y., 1970: Some basic formulations in numerical variational analysis. Mon. Wea. Rev., 98, 875-883.

Sashegyi, K. D., and R. V. Madala, 1994: Initial conditions and boundary conditions. In Mesoscale Modeling of the Atmosphere, R. A. Pielke and R. P. Pearce (Eds), Meteor. Mono., Vol. 25, No. 47, 1-12.

Schoenstadt, A. L., 1978: A transfer function analsysis of numerical schemes used to simulate geostrophic adjustment. NPS Rept. NPS-53-79-001, 44pp.

Schumann, T. E. W., 1950: The fundamentals of weather forecasting. Weather, 5, 220-224.

Shapiro, R. 1970: Smoothing, filtering, and boundary effects. Rev. Geophys. And Space Phys., 8, 359-387.

Shapiro, R., 1975: Linear filtering. Math. Compu., 29, 1094-1097.

Sivillo, J. K., J. E. Ahlquist, and Z. Toth, 1997: An ensemble forecasting primer. 12, 809-818.

Skamarock, W. C., 1989: Truncation error estimates for refinement criteria in nested adaptive models. Mon. Wea. Rev., 117, 872-886.

Skamarock, W. C., and J. B. Klemp, 1993: Adaptive grid refinement for 2-D and 3-D nonhydrostatic atmospheric flow, 121, 788-804.

Skamarock, W. C., and J. B. Klemp, 1994: Efficiency and accuracy of the Klemp-Wilhelmson time-splitting technique. 122, 2623-2630.

Skamarock, W. C., J. B. Klemp, and J. Dudhia, 2001: Prototypes for the WRF (Weather Research and Forecast) model. Ninth Conf. Meso. Processes, Amer. Meteor. Soc., J11-15, 30 July - 2 August, Fort Lauderdale, FL.

Skamarock, W. C., J. Oliger, and R. L. Street, 1989: Adaptive grid refinement for numerical weather prediction. J. Compu. Phys., 80, 27-60.

Smagorinsky 1969: Problems and promises of deterministic extended range forecasting. Bull. Amer. Meteor. Soc., 59, 286-311.

Smagorinski, J., J. L. Holloway, Jr., and G. D. Hembree, 1967: Prediction experiments with a general circulation model. Proceed.. Int'l. Sympo. Dynamics Large Scale Atmospheric Processes, Nauka, Moscow, U.S.S.R., 70-134.

Sugi, M., 1986: Dynamic normal mode initialization. J. Meteor. Soc. Japan, 64, 623-632.

Sommerfeld, A., 1949: Partial Differential Equations in Physics. Academic Press, 335pp.

Stephens, J., 1970: Variational initialization of the balance equation. J. Appl. Meteor., 9, 732-739.

Sun, J., and N. A. Crook, 1996: Comparison of thermodynamic retrieval by the adjoint method with the traditional retrieval method. Mon. Wea. Rev., 124, 308-324.

Talagrand, O., 1972: On the damping of high-frequency motions in four-dimensional assimilation of meteorological data. J. Atmos. Sci., 29, 1571-1574.

Tapp, M. C., and P. W. White, 1976: A nonhydrostatic mesoscale model. Quart. J. Roy. Meteor. Soc., 102, 277-296.

Temperton, C., 1976: Dynamic initialization for barotropic and multilevel models. Quart. J. Roy. Meteor. Soc., 102, 297-311.

Temperton, C., 1988: Implicit normal mode initialization. Mon. Wea. Rev., 116, 1013-1031.

Tennekes, H., and J. L. Lumley, 1972: *A First Course in Turbulence*. The MIT Press, 300pp.

Toth, Z., and E. Kalnay, 1993: Ensemble forecasting at NMC: The generation of perturbations. Bull. Amer. Meteor. Soc., 74, 2317-2330.

Turpeinen et al. 1990: static method for assimilating rainfall ..???

Wang, T.-A., 1996: Mechanisms of wave ducting and severe downslope windstorms in a structured shear flow. Ph.D. dissertation, North Carolina State University, Raleigh, NC, 218pp.

Wang and Warner 1988: latent heating nudging

Zou, X. and Y.-H. Kuo, 1996: Rainfall assimilation through an optimal control of initial and boundary conditions in a limited-area mesoscale model. Mon. Wea. Rev., 124, 859-2882.